

Constraining the Matter Power Spectrum during Reionization and Ionospheric Errors

Sabrina Berger



Department of Physics, McGill Space Institute
McGill University
Montréal, Québec, Canada

March 11, 2022

A thesis presented for the degree of Masters of Physics

©2021 Sabrina Berger

Abstract

Two diverse research topics in radio astronomy are described in this thesis with applications to reionization and fast radio burst localization. Reionization is the era in our universe's history in which UV photons from the first galaxies reionized the universe. Fast radio bursts (FRBs) are short and extremely luminous radio transients initially observed in 2007 that are highly dispersed. Although initially seeming unrelated, these two areas may show synergistic promise in the future. FRBs could help constrain the astrophysics of reionization using their characteristic dispersion measure.

We describe a method to explore the first reconstruction of the full posterior distribution of the matter density field during reionization from 21-cm brightness temperature measurements. This will allow future 21-cm interferometric experiments to use their brightness temperature measurements to predict the structure of our universe during reionization.

We also present preliminary exploration of the use of Global Navigation Satellite Systems (GNSS) satellites to calibrate very long baseline interferometry (VLBI). The ionosphere

acts to distort and delay radio signals as they travel to telescopes on Earth. Due to the sub-nanosecond precision required with VLBI at FRB frequencies, a calibrator above the ionosphere is needed to measure this delay in real time. The use of GNSS satellites is motivated by the lack of steady state calibrations at low frequencies with the upcoming Canadian Hydrogen Intensity Mapping Experiment (CHIME) Outriggers and future VLBI instruments. This will contribute to eventual milliarcsecond localization of FRBs within galaxies with CHIME Outriggers. By precisely localizing FRBs, we may be able to better discern their progenitors.

Abrégé

Deux sujets de recherche variés en radioastronomie sont décrits dans cette thèse avec des applications à la réionisation et à la localisation des sursauts radio rapides. La réionisation est l'époque de l'histoire de notre univers au cours de laquelle les photons UV des premières galaxies ont réionisé l'univers. Les sursauts radio rapides (FRB) sont des phénomènes transitoires radio courts et extrêmement lumineux, observés pour la première fois en 2007 et très dispersés. Bien qu'ils semblent initialement sans rapport, ces deux domaines pourraient s'avérer synergiques et prometteurs à l'avenir. Les FRBs pourraient aider à contraindre l'astrophysique de la réionisation en utilisant leur mesure de dispersion caractéristique.

Nous décrivons une méthode permettant de réaliser la première reconstruction de la distribution postérieure complète du champ de densité de matière pendant la réionisation à partir de mesures de la température de brillance à 21 cm. Cela permettra aux futures expériences interférométriques à 21 cm d'utiliser leurs mesures de température de brillance pour prédire la structure de notre univers pendant la réionisation.

Nous présentons également une exploration préliminaire de l'utilisation des satellites du Global Navigation Satellite Systems (GNSS) pour calibrer l'interférométrie à très longue base (VLBI). L'ionosphère a pour effet de déformer et de retarder les signaux radio lorsqu'ils sont transmis aux télescopes sur Terre. En raison de la précision sub-nanoseconde requise par l'interférométrie à très longue base aux fréquences des FRB, un calibrateur au-dessus de l'ionosphère est nécessaire pour mesurer ce retard en temps réel. L'utilisation de satellites GNSS est motivée par le manque d'étalonnages en régime permanent à basse fréquence avec les futurs instruments de VLBI et les prochains outriggers de l'expérience canadienne de cartographie de l'intensité de l'hydrogène (CHIME). Cela contribuera à une éventuelle localisation à la milliarcseconde des FRBs dans les galaxies avec les outriggers de CHIME. En localisant précisément les FRBs, nous pourrions peut-être mieux discerner leurs origines.

Acknowledgements

I would first like to thank my wonderful advisors during my MSc. Adrian Liu, Jonathan Sievers, Mubdi Rahman, and Vicky Kaspi guided me through the process of finishing my MSc thesis. Although I won't be continuing to work closely with Adrian for my PhD, I have genuinely enjoyed my time doing research with him. He's been an honest and caring mentor to me the last two years, and I still feel extremely grateful to him for accepting my MSc application in 2019. I feel extremely fortunate to have gotten to work under such intelligent and kind scientists.

I would also like to thank Leslie Rogers for her continued guidance and support throughout my undergraduate and graduate studies. Leslie has been instrumental in many of my accomplishments throughout the years. Her mentorship has also been vital in my self-esteem as a scientist and also shown me how justice, kindness, and compassion can only further the strength of a scientist.

Thank you to all my lovely friends in Montréal and abroad. As cliché as it sounds, the frigid Montréal winter was made less cold with your presence. Lastly, thank you to some

of the most empathetic, sensitive, and kind people I know: my father, Don Berger, all too similar sister, Samantha Berger, and grandmother, Elizabeth Berger, whose advice and grit through whatever life throws their way have helped me find my way through mine.

Contents

List of Figures	1
1 Epoch of Reionization: Setting the Stage	2
1.1 Introduction to Reionization and FRBs	2
1.2 The Initial Conditions for Structure Formation	4
1.2.1 The Formation of the CMB	4
1.2.2 The Angular Power Spectrum and CMB Anisotropies	5
1.3 Creating the Final Conditions for Large Scale Structure Formation	9
1.3.1 The Matter Power Spectrum of the Dark Ages	9
1.3.2 The First Objects to Collapse	11
1.3.3 Complex Structures Emerge through Reionization	13
1.4 Probes of Reionization	15
2 Using the 21-cm Line to Probe Reionization	18
2.1 21-cm Cosmology	18

2.2	Radiative Processes of 21-cm Cosmology	20
3	A Bayesian Model for 21-cm Observations	24
3.1	Bayes' Theorem	25
3.2	Monte Carlo Methods to Sample Posteriors	27
3.3	Hamiltonian Monte Carlo	27
3.4	A Simplified Likelihood for a Toy Model of Density Fields	32
3.5	An Analytic Likelihood Function for Density Fields	39
4	Predicting the Matter Density Field during Reionization	44
4.1	Initial Attempt with <i>emcee</i>	46
4.2	Density Error Estimates with HMC	49
4.3	Comparing Theoretical and Predicted Power Spectra	54
4.4	Future Large Scale 3D Density Field Posteriors	57
5	The Ionosphere and Low-Frequency Radio Astronomy	59
5.1	Plasma Frequency Derivation	61
5.2	Ionospheric Differentiation and Formation	67
5.3	The Ionosphere and Radio Astronomy	69
5.3.1	First Order Effects	69
5.3.2	Second Order Effects	70

6 Pulsars as Calibrators	79
6.1 Ideal Pulsar Calibrators	82
6.2 Combining CHIME and ATNF Pulsar data	83
6.3 Pulsar S/N	84
6.4 Localization Precision	87
6.5 Scattering Angle	90
6.6 Results	91
7 GNSS Satellites: A novel VLBI calibration method	93
7.1 GNSS Antenna Prototype	96
7.2 Methods	99
8 Conclusion	106

List of Figures

- 1.1 A Mollweide projection of the cosmic microwave background showing temperature fluctuations (anisotropies) about 2.7 K observed by the Planck telescope. The grey outline shows the confidence mask for particularly bright regions, such as the galactic center. Credit: ESA and the Planck Collaboration 5
- 1.2 Modified figure of the angular power spectrum from the most recent Planck measurements (from [1]). The light we overplotted on the figure is the Λ CDM theoretical model. The bottom panel shows the residuals with respect to this model. 8
- 1.3 This plot shows the evolution of the filtering mass and Jeans mass (dot-dashed line) with redshift. The global average of the filtering mass is in the thick solid line. The other solid, dashed and dotted lines show the filtering mass with respect to redshift for relative velocities between the baryons and dark matter equal to 0, 1σ , and 2σ , respectively. Credit: [2]. 13

1.4	A snapshot from the famous Millenium Simulation at redshift of 18.3 or 0.21 Gyr after the Big Bang. The simulation traced more than 10 billion particles over Gigayears. Credit: Springel et al. (2005)	14
1.5	Various reionization probes as a function of redshift along with their corresponding neutral fraction constraints. This figure is [3] which describes constraining reionization between z at about 6 and 7 with Ly α luminosity functions.	16
2.1	A graphic depicting the emission of a 21-cm photon. Credit: http://hyperphysics.phy-astr.gsu.edu/	19
3.1	An example of the gradient of the posterior without any momentum added from [4]	29
3.2	A satellite orbiting Earth with enough momentum to stay in a stable orbit from [4]	30
3.3	A two pixel universe application of <i>emcee</i> with our toy model. We used two brightness temperatures equal to 5 and 11 mK for the first and second pixel, respectively. Note that the α parameter is assumed to be in mK as we assume densities without units in this case.	38

3.4	The correlation (left) and bias (right) as a function of redshift are shown for various RadHydro simulations. The orange and light green lines on the right plot show the extremes of the bias function for long and short reionization, respectively. Both plots are from [5]	41
4.1	Overview of 1D density field at redshift = 10 for <i>emcee</i> . The black dashed line is the actual matter density field. The yellow regions are the ionized regions of the density field. Walkers are started very close to their actual values which leads to convergence to the actual density field. The span of the turquoise points here represent a pseudo-error bar that is an underestimate.	47
4.2	The same plot as 4.1 but for redshift = 8.	48
4.3	A similar plot to 4.1 where walkers are initialized completely randomly in a neutral universe at redshift = 15.	49
4.4	A completely neutral universe's density field at redshift = 17 predicted the HMC. The turquoise band around the truth densities again represents the rough errors of the predicted densities. Compared to figure 4.3, the HMC walkers converge easily.	50
4.5	A universe's density field with three ionized pixels seen in yellow at redshift = 12 predicted by the HMC. Compared to figure 4.4 which was sampled the same amount, the HMC walkers no longer converge to the proper densities.	52
4.6	Similar to figure 4.5 but at 32 pixels. We show the last 1000 samples.	53

-
- 4.7 The difference between the actual density field and sampled density fields are shown in this plot for the last 100 samples are shown in this plot. 54
- 4.8 Corresponding to figure 4.4 spectra for the 1000 last samples ($P_{constructed}$), the true density field (P_{true}), and the power spectra we determine if we set all ionized pixels to 0 ($P_{ionized}$). The $P_{ionized}$ spectrum is the same as P_{true} since at redshift = 17, they're completely neutral. 55
- 4.9 Similar to figure 4.8 but at redshift = 12 corresponding to the predicted density field in figure 4.6. The errors in the power spectra are notable here compared to redshift = 17. 56
- 5.1 Distilled model of free electrons in ionosphere in a simple lattice structure. Modified Image Credit: Ilene Dixon 62
- 5.2 Schematic of the layers of the ionosphere. Credit: Naval Postgraduate School 67
- 5.3 Altitude versus electron density within the ionosphere. Credit: Electronic Notes 68
- 5.4 Recent map showing the plasma (critical) frequency dependence on longitude. Frequencies below the plasma frequency will be reflected back to Earth from the ionosphere. These types of maps can be created with ionosondes, which sends various frequency pulses between about 1-22 MHz to quantify which frequencies are reflected or delayed. Credit: Australian Bureau of Meteorology 70

5.5	Skywave propagation can utilize the ionospheric index of refraction being less than 1 for frequencies closer to the plasma frequency to allow radio communication over large distances. Credit: Electronic Notes	73
5.6	Ray diagram showing frequency dependence of waves propagating through plasma in the ionosphere where f_p and n_p are the plasma frequency and plasma number density, respectively. Credit: Australian Space Academy	74
6.1	Example spectra of a few radio galaxies (top panel) and quasars (bottom panel) Credit https://ned.ipac.caltech.edu/level5/Sept04/Kellermann2/Kellermann1_3.html	81
6.2	837 pulsars from the ATNF catalog have not yet been observed by CHIME but are visible in the CHIME field of view.	89
6.3	Pulsars detectable by CHIME falling with our S/N and localization error constraints (less than 10 mas). The color denotes the scattering angle of the pulsar.	92
7.1	A depiction of an ionospheric pierce point. A signal from a satellite will cross the ionosphere at a pierce point before arriving at the receiver. Image Credit: Yury Kirienko	96
7.2	Frequency bands available for satellite observations.	97

7.3	A graphic depicting various individual stages of the GNSS satellite modulation scheme.	99
7.4	Output from GNSS SDR with BMX data and a poor acquisition.	101
7.5	Ideal output from GNSS SDR with an excellent acquisition. Credit: GNSS SDR	101
7.6	Preliminary plot of sTECs versus time using a GNSS receiver.	103

Chapter 1

Epoch of Reionization: Setting the Stage

1.1 Introduction to Reionization and FRBs

The use of radio astronomy has been key to discoveries made in cosmology for almost 100 years. It also enabled the growing field of fast radio bursts (FRBs) as evident from their name, FRBs have only been observed in the radio so far. FRBs are extremely powerful radio transients on millisecond timescales. When they go off, they are the brightest object in the radio sky. Reionization is the epoch in the universe where neutral hydrogen began to ionize between when the universe was about half a billion years old to 2.5 billion years old. This allowed the creation of the stars and galaxies visible today. However, the epoch of

reionization remains highly mysterious and not well understood. In this thesis, we present a method for constraining the matter power spectrum during reionization. This is key to understanding the matter distribution at the time of reionization. Although the topics in this thesis are varied, a synergistic relationship can be found and seems to be emerging (See [6]). Perhaps, fast radio bursts may be useful in further constraining reionization. To do so, however, localizations that are orders of magnitude more precise will most likely need to be made on fast radio bursts themselves.

In chapters 1.1 to 4, we describe a novel way to derive the density field at reionization redshifts from brightness temperature measurements. This density field construction includes a full posterior distribution of the field at each pixel to place error bar constraints on the predicted density. In chapters 5 to 7, a novel technique to use GNSS satellites to place better constraints on fast radio burst localizations is described. This thesis may seem to be a relatively obvious astrophysical potpourri, but perhaps the link between the two may be stronger than we previously thought and will become more evident in future years. This thesis considers both an experimental and theoretical problem to leverage the power of radio astronomy.

1.2 The Initial Conditions for Structure Formation

1.2.1 The Formation of the CMB

If we naively trace the evolution of our universe back to 13.7 billion years ago, we arrive at a singularity. However, this is not actually accurate, and we believe that new physics occurs right before the big bang. One hypothesis holds the big bang was an inflationary period that lasted an extremely small fraction of a second in which the universe expanded exponentially. From the initial expansion to the production of the cosmic microwave background (CMB) during recombination, the mechanisms and events remain under great debate, ranging from the inflationary scenario to string gas and bouncing cosmologies [7]. Prior to a redshift of approximately 1100 (or 370,000 years after the big bang), the universe's plasma was effectively opaque. This was caused by scattering of photons off free electrons. Eventually the universe cooled to around 3000 K. This was cool enough to allow the formation of neutral hydrogen during recombination. Photons were then able to decouple from matter and travel freely. We observe the CMB's redshifted blackbody radiation at approximately 2.7 K today. However, the temperature deviations from 2.7 K can be seen in the projection showing the temperature fluctuations observed by the Planck telescope in figure 1.1. The faint radio background of the CMB is isotropic, but figure 1.1 clearly shows the anisotropic nature of the CMB in our universe. These anisotropies allowed us to uncover parts of the universe's history not previously known or understood.

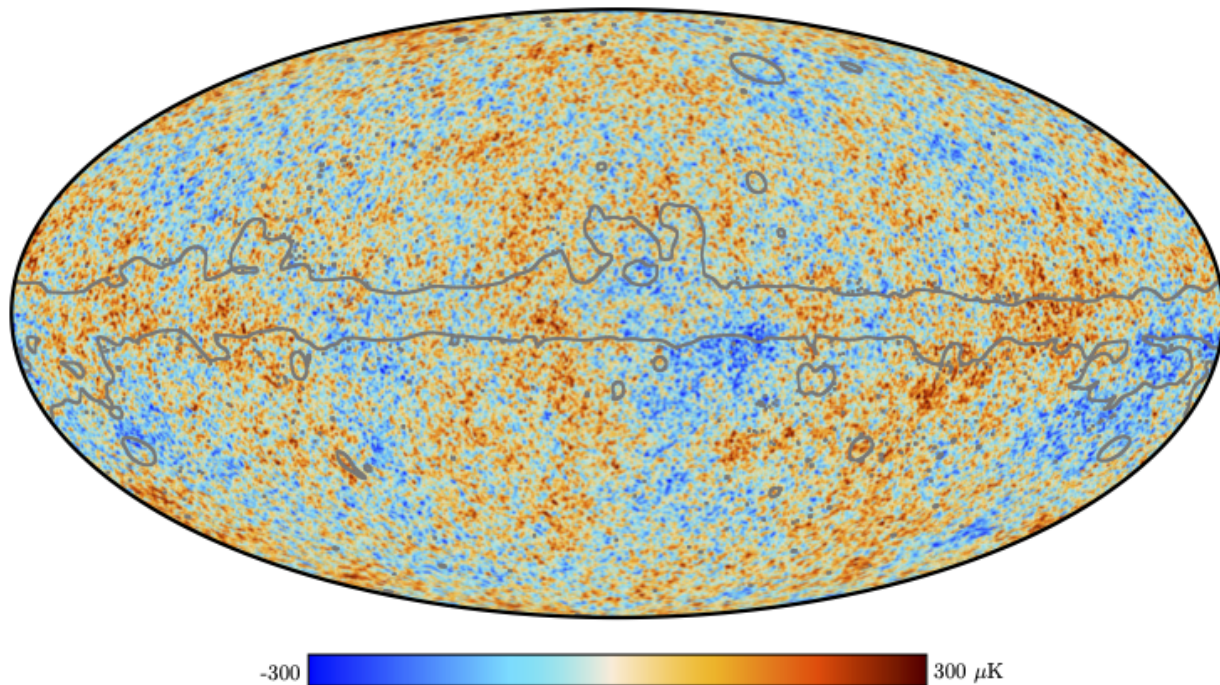


Figure 1.1: A Mollweide projection of the cosmic microwave background showing temperature fluctuations (anisotropies) about 2.7 K observed by the Planck telescope. The grey outline shows the confidence mask for particularly bright regions, such as the galactic center. Credit: ESA and the Planck Collaboration

1.2.2 The Angular Power Spectrum and CMB Anisotropies

The primary portion of CMB anisotropies are due to density fluctuations in the universe. When projecting the celestial sphere onto 2D (as is done with a Mollweide projection in 1.1), there are also projection effects causing areas to appear larger or smaller than they actually are. The other origins of the CMB anisotropies are the most cosmologically interesting and also provide the largest clues into the initial expansion of our universe, including theories

such as inflation. These can be best explored by examining the angular power spectrum (C_l) of the CMB.

A power spectrum is a Fourier transform of a correlation function. We can understand the angular power spectrum by first breaking down its components. A two-point correlation function is defined as the ensemble average of a quantity at two points in space, e.g., a two-point temperature correlation function would look like this:

$$\xi(\mathbf{r}_1 - \mathbf{r}_2) = \langle T(\mathbf{r}_1)T(\mathbf{r}_2) \rangle. \quad (1.1)$$

Here we are interested in the deviations from the average temperature of the CMB ($\langle T \rangle = 2.7K$). The dimensionless quantity to describe that deviation is:

$$\Theta(\hat{n}) = \frac{T(\hat{n}) - \langle T \rangle}{\langle T \rangle}, \quad (1.2)$$

$\hat{n} \equiv (\theta, \phi)$ is a unit vector pointing in the direction of the sky we're examining the temperature. We analyze the CMB "sphere" (existing all around us) using spherical harmonics to accurately understand the CMB. Spherical harmonics are useful in this situation to represent functions on a sphere. Spherical harmonics represent the fundamental modes of "vibration" on a sphere. We define the complete orthonormal

spherical harmonics set as:

$$Y_{lm} = \sqrt{\frac{2l+1}{4\pi} \frac{(l-m)!}{(l+m)!}} P_l^m(\cos\theta) e^{im\phi}, \quad (1.3)$$

where l and m are integers such that $l \geq 0$, $|m| \leq l$, and P_l^m are the associated Legendre polynomials. We call l the multipole; it corresponds to an angular scale of $\theta = \pi/l$. Our angular power spectrum is:

$$C_l = \frac{1}{2l+1} \sum_{m=-l}^l \langle |a_{lm}|^2 \rangle, \quad (1.4)$$

where the harmonic coefficients are defined from the dimensionless quantity, $\Theta(\hat{n})$, the complex conjugate of the spherical harmonics, and solid angle differential ($d\Omega$):

$$a_{lm} = \int_{\theta=-\pi}^{\pi} \int_{\phi=0}^{2\pi} \Theta(\hat{n}) Y_{lm}^*(\hat{n}) d\Omega. \quad (1.5)$$

Using the most recent measurements using the Planck instrument, the angular power spectrum plotted with data points and a best fit is displayed in figure 1.2. It serves as the most valuable tool for understanding the history of the CMB.

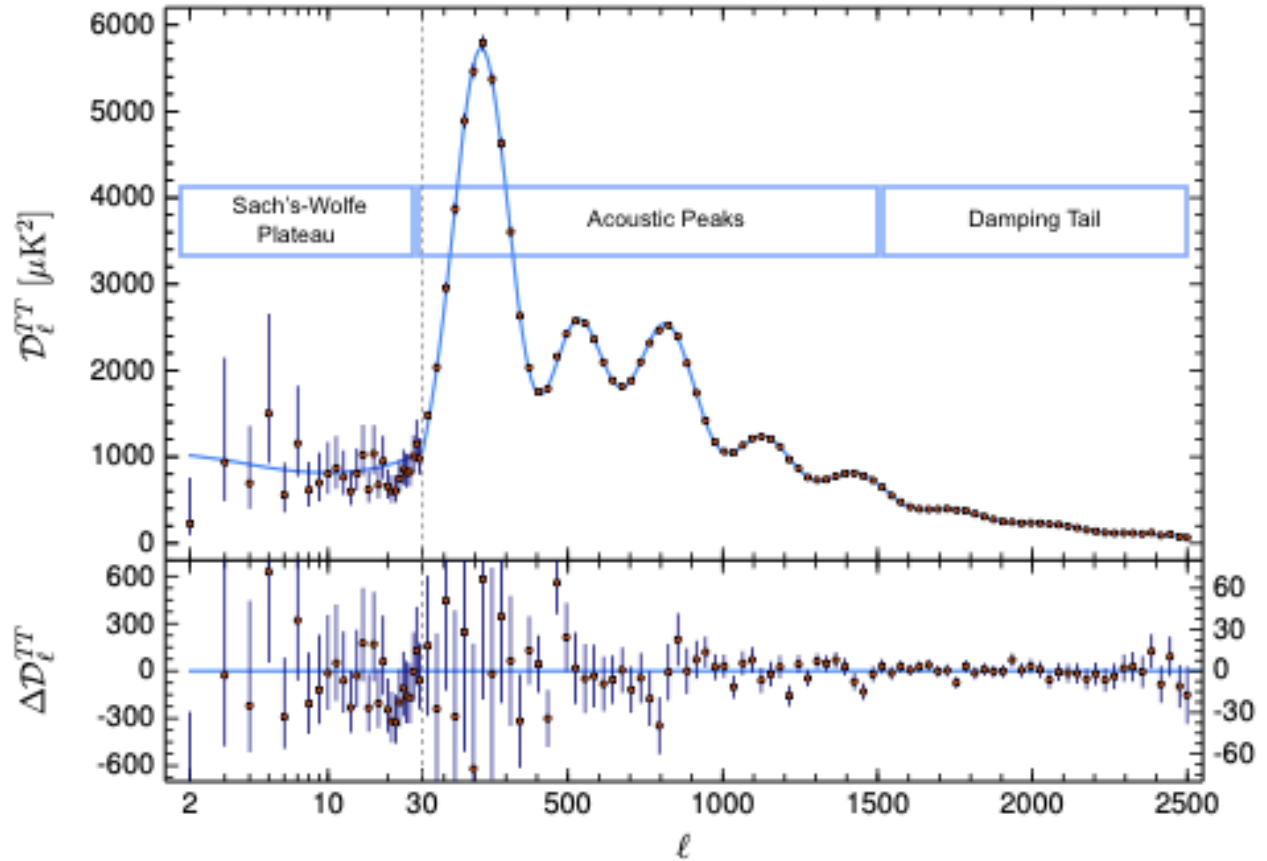


Figure 1.2: Modified figure of the angular power spectrum from the most recent Planck measurements (from [1]). The light we overlotted on the figure is the Λ CDM theoretical model. The bottom panel shows the residuals with respect to this model.

In brief, the CMB anisotropies (besides those due to primordial density fluctuations and projection effects) can be characterized from low to high multipole as the Sach’s-Wolfe plateau, acoustic peaks, and the damping tail. These are marked across their approximate multipole range in figure 1.2. The Sach’s-Wolfe effect is divided into an ordinary and integrated effect. The ordinary Sach’s-Wolfe effect is due to the effect on CMB photons of the potential wells at recombination. The integrated effect comes about because of a

change in potential as the photon passes through a potential well. It has an early and a late stage, occurring in the matter-dominated and dark-energy dominated epochs, respectively. The acoustic peaks show the position in compression or rarefaction of the photons at the time of last scattering. Lastly, the damping tail is due to the imperfection in the coupling of the photon-baryon fluid prior to decoupling.

The CMB can be used to constrain the fundamental parameters of our universe and even probe reionization. However, this thesis takes a different approach to study reionization by exploring the mapping between observations from radio telescopes and their predicted density fields.

1.3 Creating the Final Conditions for Large Scale Structure Formation

1.3.1 The Matter Power Spectrum of the Dark Ages

Between the decoupling of photons as the first neutral atoms formed and reionization, i.e., the second phase change of hydrogen, the main sources of photons were the scattered photons constituting the cosmic microwave background (CMB) and those that were released during the rare spin-flip transition of neutral hydrogen atoms. This period called the Dark Ages began around $z = 1000$ and lasted until the first stars formed. Reionization began at about $z = 11$ where neutral hydrogen was ionized allowing the formation of the stars and galaxies we

see today. Neutral hydrogen is abundant in our universe and consequently traces the matter distribution. The spin-flip transition is rare, but because of the immense quantity in our universe, we are still able to trace neutral hydrogen in our universe through this transition. Fortunately, the intergalactic medium is optically thin to the 21-cm line transition so we're able to observe the line from our telescopes on Earth. The matter power spectrum can be mapped from the neutral hydrogen emission, but this gets more difficult as more regions become ionized and do not further emit 21-cm emission. We can also map the matter power spectrum from $z \lesssim 3$ large galaxy surveys such as the Sloan Digital Sky Survey (SDSS) and the Dark Energy Spectroscopic Instrument (DESI). These galaxy surveys look at large regions in the sky to derive the matter correlation function. We describe fluctuations in the density field with:

$$\delta(\mathbf{r}_1) = \frac{\rho(\mathbf{r}_1) - \bar{\rho}}{\bar{\rho}}. \quad (1.6)$$

We can then define the matter power spectrum as:

$$P_{mm}(\mathbf{k}) = P(\mathbf{k}) = \int_{-\infty}^{\infty} d^3r e^{-i\mathbf{k}\cdot\mathbf{r}} \xi(\mathbf{r}), \quad (1.7)$$

which in our case is the Fourier transform of the two-point correlation function. The two point correlation function is the following ensemble average:

$$\xi(\mathbf{r}) = \langle \delta(\mathbf{r}_1) \delta(\mathbf{r}_2) \rangle. \quad (1.8)$$

The matter power spectra will be key in our work understanding the density field of our universe during reionization. To understand how the density field of our universe formed and evolved during reionization, it is important to consider how the dark matter traces in our universe. Dark matter evolution helps drive star formation. The formation of the first stars during reionization is a key part of this epoch.

1.3.2 The First Objects to Collapse

Population III stars, made of primordial hydrogen and helium gas are speculated to be the first star that formed but have yet to be detected. The most commonly accepted reason for their lack of detection is that no low mass Population III stars ever formed. Their masses were all higher than 100 solar masses and therefore they burned through all their hydrogen and helium quickly ([8]). Population III stars acted to both defer and hasten the onset of reionization. Their supernovae dispersed the needed gas for stars to form such that it was not concentrated enough to immediately allow star formation. However, the heavy metals created in these Population III stars were also dispersed during their transition to stellar remnants. These heavy metals could then go into higher metallicity stars that would produce more UV photons. We know that gas clouds must collapse in order to form protostars. However, metal rich clouds cool more efficiently. If we examine the Jeans mass

where if a cloud's mass is greater than the Jeans mass there will be a collapse:

$$M_J = \left(\frac{5kT}{Gm} \right)^{3/2} \left(\frac{3}{4\pi\rho} \right)^{1/2}, \quad (1.9)$$

where k is the Boltzmann constant, m is the average particle mass, T is the temperature of the cloud, and ρ is the density of the cloud. We can see that higher density, cooler clouds will have lower Jeans mass and therefore are less stable and more prone to star formation. A diffuse neutral hydrogen cloud is much more stable than a molecular cloud since it's less dense and less likely to reach the Jeans mass threshold essential for collapse. (M_{cloud} must be greater than M_J).

However, note that the Jean's mass in equation 1.9 is time-independent. We must examine the proper time-weighted mass called the *filtering mass* to fully consider the formation of the first stars. The filtering mass includes a more robust treatment of how linear density perturbations evolve into non-linear density perturbations through a comoving wave number, k_F . The filtering mass is:

$$M_F = \frac{4\pi}{3} \bar{\rho} \left(\frac{\pi a}{k_F} \right)^3, \quad (1.10)$$

where $\bar{\rho}$ is the average density and a is the scale factor of the universe. The filtering mass places a much better boundary on which clouds will be able to coalesce into stars and denser objects. Its filtering wave number, k_F integrates the history of baryonic pressure in

our universe versus just a snapshot as with the Jeans mass. A sample comparison of their calculations over redshift is shown in figure 1.3.

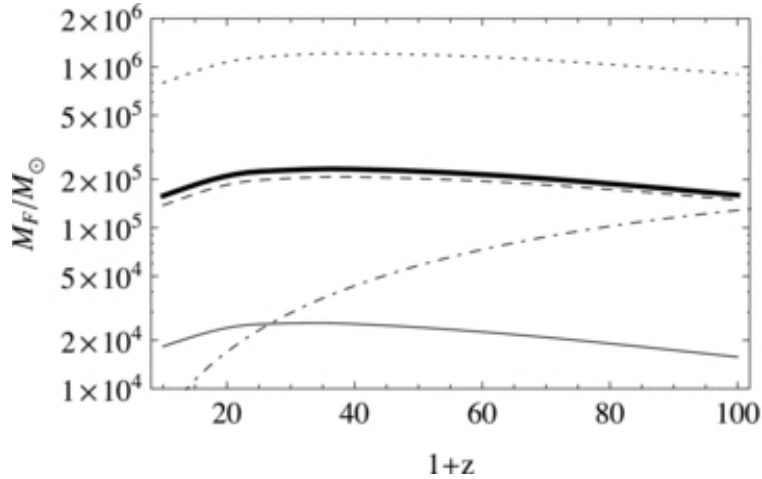


Figure 1.3: This plot shows the evolution of the filtering mass and Jeans mass (dot-dashed line) with redshift. The global average of the filtering mass is in the thick solid line. The other solid, dashed and dotted lines show the filtering mass with respect to redshift for relative velocities between the baryons and dark matter equal to 0, 1 σ , and 2 σ , respectively. Credit: [2].

The formation of the first stars therefore complicated the future of star formation. The lack of a detection of Population III stars further complicates our understanding of this era of our universe.

1.3.3 Complex Structures Emerge through Reionization

Although neutral hydrogen was created in recombination, the fragility of the hydrogen atom would not be put to the test until reionization. Prior to the initial formation of stars, the

universe was relatively simple. Now we see extreme complexity in the large scale structure of the universe. This structure probably formed in three stages. A clump of matter first collapsed along one dimension making a flat 2D sheet. Then the clump collapses along another dimension creating a twig like structure or 1D filament. The twig collapses along the third axis creating a gravitationally stable halo. This is seen in the famous Millenium simulation (See figure 1.4) where extremely dense regions form a web around voids. The dense regions are where the first galaxies and galaxy clusters formed where the dark matter halos act as drains for matter.

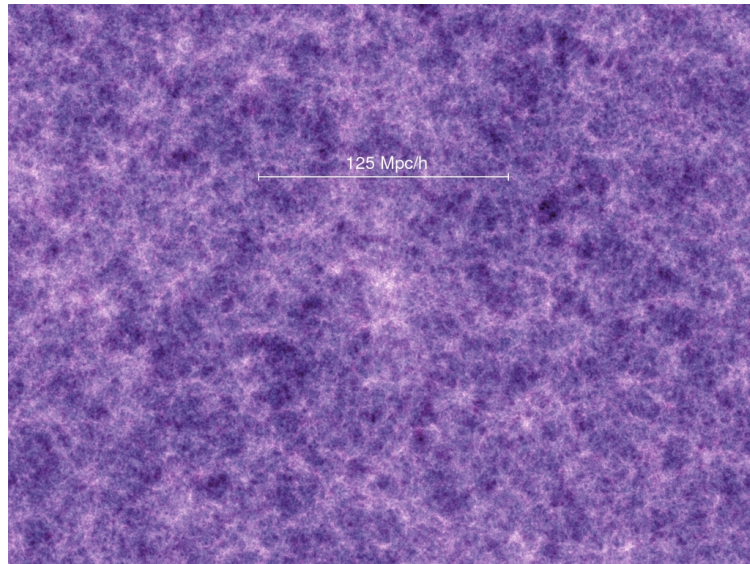


Figure 1.4: A snapshot from the famous Millenium Simulation at redshift of 18.3 or 0.21 Gyr after the Big Bang. The simulation traced more than 10 billion particles over Gigayears. Credit: Springel et al. (2005)

Once the first stars formed, they begin to produce UV photons which breaks up neutral hydrogen. This process is called ionization. The oldest stars to form with lower metallicity

but higher than Population III stars were called Population II stars. Historically, the youngest stars with the highest amount of elements heavier than Helium were called Population I stars. Quasars, supermassive black holes with extremely luminous accretion disks, also began to reionize the universe. UV photons continued to reionize the universe until the end of reionization at about $z = 5$. When we study reionization with the 21-cm line, we're left with many "gaps in our knowledge" or ionized regions that don't emit photons like their neutral counterparts. Emission from neutral hydrogen is still the key probe in our quest to understand the density field during reionization.

1.4 Probes of Reionization

Reionization took place until z was less than 10, potentially $z \gtrsim 5$ [9]. During reionization, ultraviolet (UV) photons from the birth of the first galaxies with Population II stars, quasars, and other luminous photons ionized the intergalactic medium (IGM) as described in Chapter 1. The main drivers of reionization are the first galaxies containing Population II stars as they provide sustained UV emission that allows other parts of the universe to ionize. Although we focus on the use of the 21-cm line to explore reionization here, there are many other ways to study reionization. See figure 1.5 below. Although neutral hydrogen isn't shown in this plot, we see there are many more ways to study this period.

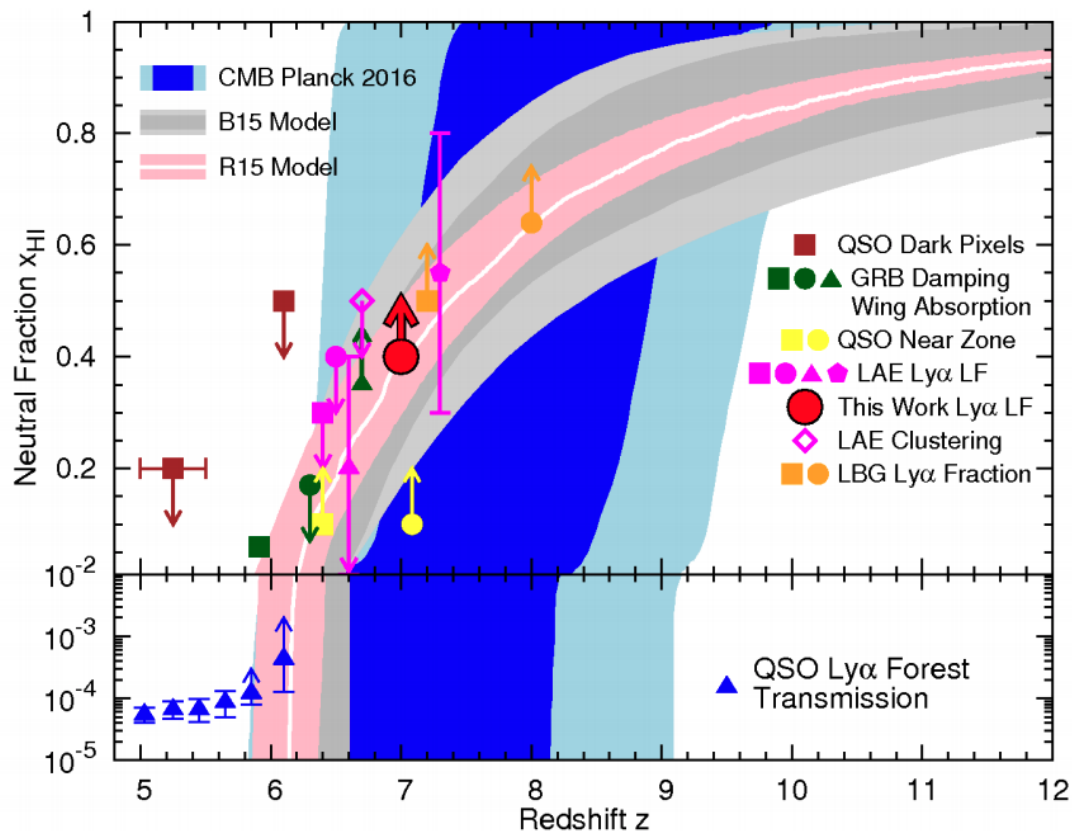


Figure 1.5: Various reionization probes as a function of redshift along with their corresponding neutral fraction constraints. This figure is [3] which describes constraining reionization between z at about 6 and 7 with Ly α luminosity functions.

This era has been studied with quasar observations, galaxy surveys, and the CMB; however, these all have drawbacks. CMB photons are Thomson scattered off free electrons during reionization. This reduces CMB photons' amplitudes and increases polarization. Converting the optical depth to reionization of the CMB into a redshift is dependent on our understanding of the electron density in the universe. This limits the precision that the redshift of reionization can be constrained with this method. Quasars can provide more

historical information on various redshifts, but their light is saturated at $z \gtrsim 6$. High-redshift galaxies face the issue of being difficult to detect. The 21-cm line of neutral hydrogen (HI) enters as a vital cosmological probe. It is not often absorbed by matter and allows us the ability to gain a 3D map of the neutral hydrogen in our universe. By studying the 21-cm line, we can trace the matter and matter velocity distribution of the intervening medium between us and the source of the 21-cm emission.

Chapter 2

Using the 21-cm Line to Probe

Reionization

2.1 21-cm Cosmology

We need to find a way to connect the matter density field to an observable quantity to be able to constrain it accurately. We use the 21-cm line for this purpose. We consider the radiative transfer of photons generated in 21-cm emission as they travel through the intergalactic medium. We employ [10] in the derivations throughout this section. The redshifted 21-cm line provides the opportunity to explore the history of reionization in three dimensions because of its spectral nature. It is also directly probing IGM gas (where its emitted). The line itself is a forbidden transition that occurs only once about 10^7 years. The ground state of

hydrogen has hyperfine structure where the nuclear and electron spins can be either parallel or antiparallel. The parallel electron and nuclear spin state has slightly higher energy than the antiparallel state. When the electron spin flips, 5.9×10^{-6} eV is emitted or equivalently, a photon of frequency $\nu = 1420 \text{ MHz}$ or $\lambda = 21 \text{ cm}$. See figure 2.1 below. The triplet state is when both spins are aligned whereas the singlet state is when one of the electron spins is flipped.

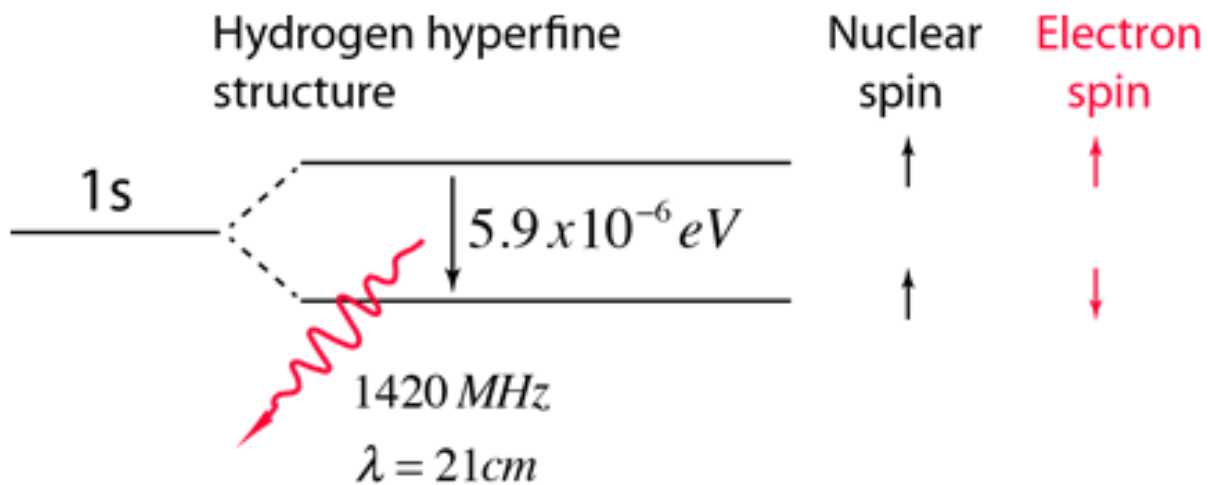


Figure 2.1: A graphic depicting the emission of a 21-cm photon. Credit: <http://hyperphysics.phy-astr.gsu.edu/>

Because there is and has been so much neutral hydrogen in our universe, this ends up occurring often enough to map the universe. There are many radio interferometric instruments to explore this spectral line currently online or in commission, including the Low Frequency Array (LOFAR, [11]), Hydrogen Epoch of Reionization Array

(HERA, [12]), and the Murchison Widefield Array (MWA, [13]). Reionization is an extremely important period of our universe, and the redshifted 21-cm spectral line gives us an ideal way to study it. The radiative processes associated with the 21-cm line are complex and provide ample ground for interesting calculations.

2.2 Radiative Processes of 21-cm Cosmology

Rather than dealing in intensities, we find the brightness temperature of the 21-cm signal is the most convenient probe in quantifying it. This is defined from the specific intensity (I_ν) of a blackbody. We are working at cosmological scales, such that we need to consider the redshift dependence of the brightness temperature that we observe on Earth:

$$T_{b,Earth}(\nu) = T'_{b,emitter}(\nu_0)/(1+z), \quad (2.1)$$

where ν and z are frequency and redshift, respectively.

The frequency on Earth is observed as

$$\nu = \nu_0/(1+z). \quad (2.2)$$

For the lower frequencies we work with in 21-cm cosmology, the Rayleigh-Jeans formula

works very well to approximate the blackbody or Planck curve:

$$B_\nu(T) = \frac{2\nu^2 kT}{c^2} \quad (2.3)$$

where k is Boltzmann constant and c is the speed of light.

For a blackbody, the brightness temperature is determined from Planck's law by solving for T from:

$$I_\nu = \frac{2h\nu^3}{c^2} \frac{1}{e^{\frac{h\nu}{kT}} - 1}, \quad (2.4)$$

but with the Rayleigh-Jean's approximation, it can be simplified to:

$$T_b = \frac{I_\nu c^2}{2\nu^2 k}. \quad (2.5)$$

Our classic radiative transfer equation in terms of brightness temperature is [9]:

$$T'_b(\nu) = T_{ex}(1 - e^{-\tau_\nu}) + T'_R(\nu)e^{-\tau_\nu}, \quad (2.6)$$

where T_{ex} is the excitation temperature of the cloud, T'_R is the brightness temperature of the radiation in which the cloud lies in along the ray passing through, and the optical depth, τ_ν is the integral of the absorption coefficient (α_ν) along the ray:

$$\tau_\nu \equiv \int \alpha_\nu ds, \quad (2.7)$$

where s is the proper distance through the integration.

T_{ex} is referred to as the spin temperature, T_s , which is used to help quantify the ratios between the triplet (1) and singlet (0) states. The spin temperature is defined via:

$$\frac{n_1}{n_0} = \frac{g_1}{g_0} e^{-E_{10}/(kT_s)} = 3e^{-T_*/T_s}, \quad (2.8)$$

where $E_{10} = 5.9 \times 10^{-6}$ is the splitting energy, g_1 and g_0 are the statistical weights of the states, and T_* is the equivalent energy. g_1 and g_0 are 1 and 3, respectively. $T_* = E_{10}/k = 0.068K$. T_s will always be much larger than T_* and so approximately 3/4 of atoms are in the triplet or excited state. This leads to a correction in our absorption coefficient and a revised optical depth as follows:

$$\tau_\nu = \int \sigma_{01}(1 - e^{-E_{10}/kT_s})(\phi(\nu))n_0 ds, \quad (2.9)$$

where

$$\sigma_{01} = \frac{3c^2 A_{10}}{8\pi\nu^2}. \quad (2.10)$$

A_{10} is the Einstein coefficient for spontaneous emission of the 21-cm transition; this is equal to the transition rate of the spin-flip transition: $A_{10} = 2.85 \times 10^{-15} s^{-1}$. $\phi(\nu)$ is the line profile [9].

We've defined some radiative processes of 21-cm cosmology, but we're really interested

in the difference in brightness temperature between the 21-cm line and the CMB in a cloud. Observational techniques try to find the 21-cm line by looking for this brightness temperature difference:

$$\delta T_b(\nu) = \frac{T_s - T_\gamma(z)}{1+z} (1 - e^{-\tau_{\nu 0}}), \quad (2.11)$$

where T_γ is the CMB temperature. $\delta T_b(\nu)$ is the 21-cm brightness temperature offset from the CMB temperature. The more pertinent relationship in this work is:

$$\delta T_b(\nu) \approx 27 X_{HI} (1 + \delta_{nl}) mK. \quad (2.12)$$

This is a simplified version as a function of the density field (δ_{nl}) but is essential for constraining the matter density field during reionization. This is the connection between observation and density that we will use later on. Chapter 3 will describe how we can exploit future brightness temperature measurements with a combination of Bayesian inference and semi-analytic simulations. This will take us closer to our goal of deriving the matter power spectra.

Chapter 3

A Bayesian Model for 21-cm

Observations

In this chapter, we give a brief overview of the fundamentals of Bayesian statistics and some methods to sample the posterior without solving for it analytically. We then walk through the development of the posterior for a toy model Gaussian likelihood describing the relationship between fluctuations of temperature and density. We show the full derivation of the analytic posterior for this toy universe. we then move on to a more realistic likelihood for inferring the temperature brightness fluctuation field from the matter density field. This is what we use in chapter 4 to predict the matter density field during reionization.

3.1 Bayes' Theorem

In the most simplistic way, Bayes' theorem describes the probability of event A occurring given what we know about event A and a separate event B. These do not have to be events, however, and in astrophysics, it's commonly the inference of parameters that we're predicting given some data. We can use it to predict discrete events as well as probability distributions. We can state this more formally with Bayes' theorem, and its derivation is quite trivial. We know that the probability of event A and B both happening lies at the intersection (\cap) of the probabilities of A and B happening: $P(A \cap B)$. If we divide this by $P(A)$, we find the probability of event B happening given ($|$) that A has occurred: $P(B|A)$. We know the following is true

$$P(B|A) = P(A \cap B)/P(A), \quad (3.1)$$

and thus the following is equally true

$$P(A|B) = P(A \cap B)/P(B). \quad (3.2)$$

Dividing the two, we find Bayes' theorem:

$$P(A|B) = \frac{P(B|A)P(A)}{P(B)}. \quad (3.3)$$

$P(A)$ and $P(B)$ are the prior and evidence, respectively. We call $P(B|A)$ the likelihood, and our final result is the posterior: $P(A|B)$. From an astrophysical perspective, we can understand Bayes' theorem as follows,

$$P(\text{theory}|\text{data}) = \frac{P(\text{data}|\text{theory})P(\text{theory})}{P(\text{data})}. \quad (3.4)$$

In this thesis, we are most interested in the following use of Bayes' theorem where we find the probability of a density given a brightness temperature measurement, i.e., the posterior distribution:

$$P(\boldsymbol{\delta}|\mathbf{T}) = \frac{P(\mathbf{T}|\boldsymbol{\delta})P(\boldsymbol{\delta})}{P(\mathbf{T})}, \quad (3.5)$$

where $P(\mathbf{T}|\boldsymbol{\delta})$ is the likelihood, $P(\boldsymbol{\delta})$ is the prior, and $P(\mathbf{T})$ is the evidence. We're inferring the way matter was distributed from measurements of the 21-cm line at reionization redshifts.

The underlying complexities of the prior, evidence, likelihood, and posterior are evident; it is not at all trivial to derive each of these components. We oftentimes leave off the evidence in our use of Bayes' theorem. We can think of the prior informing the likelihood which helps us derive the posterior distribution we set out to find. Bayes' theorem (3.3) remains a powerful tool and creates the framework of the results of this thesis.

3.2 Monte Carlo Methods to Sample Posteriors

A close companion of Bayes' theorem is the Monte Carlo Markov Chain (MCMC) which allows a numeric derivation of the posterior. An analytic computation of the posterior is rarely viable because of the complexity and lack of closed form solution of the posterior. MCMC is one way to construct a probability density distribution. We draw samples from the posterior and allow the histogram of those samples to describe our the posterior. We start with the ensemble sampler *emcee* ([14]) to perform our MCMCs. *emcee* uses the "stretch move" ensemble method described in [15] to sample the posterior. *emcee* serves as the initial try for our estimations of the density fields throughout this work. It should be highlighted that it is only computationally efficient on smaller parameter spaces, i.e., on order of 10 parameters or fewer. We exclusively explore a 1D universe in this thesis to reduce computation time. When moving to the realistic 3D universe, a different sampling technique must be used to remain computationally feasible. The Hamiltonian Monte Carlo (HMC) technique will be show in chapter 4 as a potential solution for the higher dimensional problem.

3.3 Hamiltonian Monte Carlo

We find that the MCMC described in the previous section fails quickly as we go to higher dimensions. We turn to a method that employs a gradient based sampling method to make

convergence at higher dimensions possible. The *emcee* methods discussed before will not succeed in high-dimensions when there are exponentially many ways the sampler can choose from the posterior. The *emcee* sampler is too slow to converge in a reasonable time frame. We avoid this by employing the gradient of the likelihood in a Hamiltonian Monte Carlo (HMC) with the NO U-Turn (NUTS) sampler available through *PYMC3* ([16]). Its statistical backend is Theano [17], a statistical and machine learning package which enables fast differentiation. HMC works well on large quantities of parameters because sampling of the posterior is made faster through an analytic gradient of the likelihood ([4]). The HMC uses a Hamiltonian framework where the likelihood acts as the Hamiltonian potential. Differential geometry is required to understand why it performs so well on a mathematical level, but this will not be discussed here.

HMC's ability to jump to regions of higher probability by following the gradient of the likelihood is key to deriving the matter density field. As we see in the subsequent section, we can derive a likelihood function that allows us to differentiate analytically. HMC emulates a classical mechanics problem of Hamiltonian evolution in its methods. The Hamiltonian (H) is the total energy of a system. For example, a simple point mass would have the following Hamiltonian:

$$H = K + V, \tag{3.6}$$

with corresponding kinetic and potential energies: $K = \frac{p^2}{2m}$ and V .

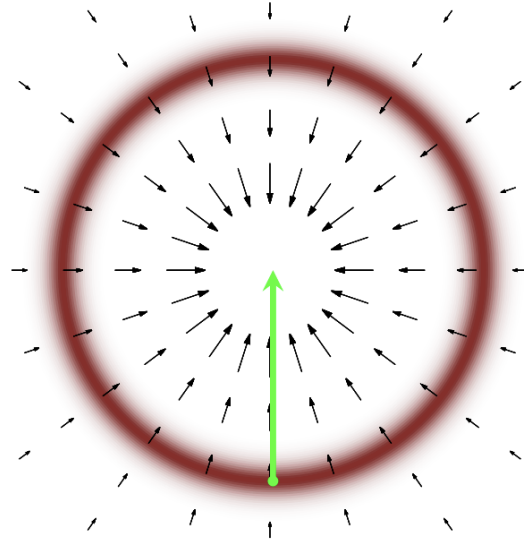


Figure 3.1: An example of the gradient of the posterior without any momentum added from [4]

HMC uses the Hamiltonian and also preserves the volume of position-momentum phase space. A momentum parameter, p_n , is introduced to account for this and to guide the gradient towards the target without crashing into the mode of the density distribution as seen in figure 3.1.

For an example physical system with a GNSS satellite orbiting the Earth with the perfect amount of momentum, 3.2 shows the evolution of a satellite in orbit and traces of potential orbits. The satellite does not crush into the Earth as it would with no momentum. This situation is analogous to the momentum parameter that's tweaked throughout the sampling done in an HMC and exemplifies its importance in this technique.

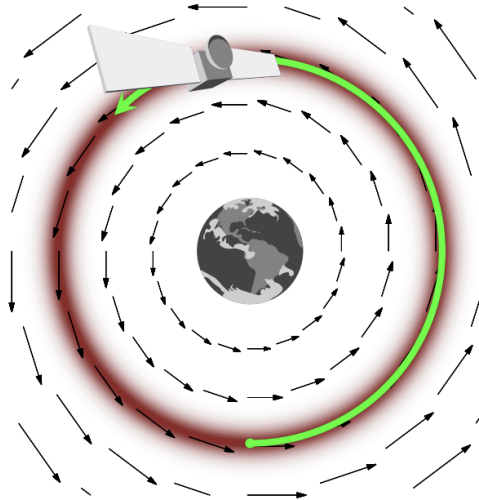


Figure 3.2: A satellite orbiting Earth with enough momentum to stay in a stable orbit from [4]

We have the following probability distribution over both momentum and the parameters we want to find (q , or overdensities at many pixels in our case):

$$\pi(q, p) = \pi(p|q)\pi(q). \quad (3.7)$$

When we marginalize over the momentum, we note that we're left with the target distribution, i.e., $\pi(q)$.

We can rewrite $\pi(q, p)$ in terms of a Hamiltonian function, $H(q, p)$:

$$\pi(q, p) = e^{-H(q, p)} \quad (3.8)$$

Logging both sides:

$$H(q, p) \equiv -\log\pi(q, p) \quad (3.9)$$

We can then decompose this into two terms to represent kinetic and potential energy:

$$H(q, p) = -\log\pi(p|q) - \log\pi(q), \quad (3.10)$$

Just as we saw for the point mass where the kinetic energy is dependent on both the momentum and mass, we see that the potential energy term is determined completely by the parameter distribution while the kinetic energy term has both a momentum and parameter dependence:

$$H(q, p) = K(p, q) + V(q). \quad (3.11)$$

Lastly, we can determine the vector field that our sampler follows in the HMC from Hamilton's equations:

$$\frac{dq}{dt} = \frac{\partial K}{\partial p} \quad (3.12)$$

$$\frac{dp}{dt} = -\frac{\partial K}{\partial p} - \frac{\partial V}{\partial p}. \quad (3.13)$$

$\frac{\partial V}{\partial p}$ is the gradient of the likelihood that will be described in the next section.

The NUTS sampler within *PYMC3* uses an expansion of each trajectory that can be found from Hamilton's equations and a slice sampler to sample from within each trajectory.

It helps users bypass the issue of selecting the step size and number of steps. With too large of a step size, the sampler is inefficient at properly sampling the posterior, and with too small of a step size, the HMC remains a random walk that is similar to traditional MCMC sampling methods. There is a fine balance between step size and efficiently sampling the posterior through HMC. NUTS (first explored in [18]) uses a recursive algorithm that doesn't allow the sampler to trace over points already tried, i.e., no U-turns. It performs at least as well if not better than a hand-tuned HMC.

3.4 A Simplified Likelihood for a Toy Model of Density Fields

As described in chapter 1.1, determining the density field from 21-cm brightness temperature measurements is a key part of understanding the reionization of our universe and is the core result of the cosmology part of this thesis. We begin with a **toy model** derivation of the posterior of a 1-pixel universe as a way to demonstrate an explicit derivation of the posterior for HMC. We note that this is truly a 1 pixel toy model for our universe where we use just one value for density to describe it. We take the simple model

$$\mathbf{T} = \alpha \delta^2, \tag{3.14}$$

alwhere \mathbf{T} is the brightness temperature vector (in this case all vectors describe the 1-pixel universe and are therefore scalars), α is a constant, and δ is the density pixel. This model was chosen because of its non-linear dependency on density which resembles the real density and temperature brightness distribution. It also allows for an analytic gradient to be taken easily and tried with an HMC.

Equation 3.14 leads to a likelihood where we assume no instrumental noise, enabling us to employ the Dirac delta function:

$$P(\mathbf{T}|\delta, \alpha) = \delta^D(\mathbf{T} - \alpha\delta^2), \quad (3.15)$$

remembering that

$$\delta^D(\mathbf{T} - \alpha\delta^2) = 0, \quad (3.16)$$

when,

$$\mathbf{T} \neq \alpha\delta^2. \quad (3.17)$$

As we saw in section 3.1, we want to understand the posterior of the matter density field from measurements of the brightness temperature. We rewrite equation 3.5 to include the nuisance parameter, α , from the toy model:

$$P(\delta, \alpha|\mathbf{T}) = \frac{P(\mathbf{T}|\delta, \alpha)P(\delta, \alpha)}{P(\mathbf{T})}. \quad (3.18)$$

Again, where $P(\mathbf{T}|\boldsymbol{\delta}, \alpha)$ is the likelihood, $P(\boldsymbol{\delta}, \alpha)$ is the prior, and $P(\mathbf{T})$ is the evidence.

Although the posterior will not be normalized, we initially leave off the evidence because we assume a perfect instrument does the observations:

$$P(\boldsymbol{\delta}, \alpha|\mathbf{T}) \propto P(\mathbf{T}|\boldsymbol{\delta}, \alpha)P(\boldsymbol{\delta}, \alpha). \quad (3.19)$$

We know we could eventually normalize the posterior with a division by $P(\mathbf{T})$ as seen in equation 3.18. We could find our normalization factor this way:

$$P(\mathbf{T}) = \int \int P(\mathbf{T}, \boldsymbol{\delta}, \alpha)d\boldsymbol{\delta}d\alpha. \quad (3.20)$$

However, we also know that

$$P(A, B) = P(A|B)P(B), \quad (3.21)$$

and

$$P(\mathbf{T}) = \int \int P(\mathbf{T}|\boldsymbol{\delta}, \alpha)P(\boldsymbol{\delta}, \alpha)d\boldsymbol{\delta}d\alpha. \quad (3.22)$$

Note that we assume the one-pixel universe case and replace our vectors with scalars.

This is the marginalized version of the right hand side of equation 3.19 over $\boldsymbol{\delta}$ and α . If we were to sample from the posterior using a Monte Carlo technique that will be discussed soon, we would be equivalently applying this marginalization and normalizing the posterior. The evidence itself contains none of the parameters we're interested in, and we can easily

normalize our posteriors by remembering that they must integrate to 1.

We assume a Gaussian distribution for the prior. The Gaussian probability distribution of α and δ are multiplied to find the equivalent probability of both the parameters with standard deviations σ_α and σ_δ :

$$P(\delta, \alpha) = \frac{1}{2\pi\sigma_\alpha\sigma_\delta} e^{\frac{-\delta^2}{2\sigma_\delta^2}} e^{\frac{-\alpha^2}{2\sigma_\alpha^2}}. \quad (3.23)$$

In this toy problem, however, we have a degeneracy in α and δ . We can avoid this by marginalizing over α , i.e., integrating over all possible α . We integrate from $-\infty$ and ∞ for α :

$$P(\boldsymbol{\delta}|\mathbf{T}) = \int_{-\infty}^{\infty} P(\boldsymbol{\delta}, \alpha|\mathbf{T}) d\alpha. \quad (3.24)$$

Expanding the posterior out, we find:

$$P(\boldsymbol{\delta}|\mathbf{T}) \propto \int_{-\infty}^{\infty} P(\mathbf{T}|\boldsymbol{\delta}, \alpha) P(\boldsymbol{\delta}, \alpha) d\alpha. \quad (3.25)$$

We substitute in the prior and likelihood next, again replacing the vectors with scalars because we use a one pixel universe:

$$P(\delta|T) \propto \int_{-\infty}^{\infty} \delta^D (T - \alpha\delta^2) \frac{1}{2\pi\sigma_\alpha\sigma_\delta} e^{\frac{-\delta^2}{2\sigma_\delta^2}} e^{\frac{-\alpha^2}{2\sigma_\alpha^2}} d\alpha \quad (3.26)$$

We use w-substitution to analytically solve this integral. We make the following substitutions:

$w = -\alpha\delta^2$, and $dw = -\delta^2 d\alpha$ to find:

$$P(\delta|T) \propto \frac{1}{-\delta^2} \int_{-\infty}^{\infty} \delta(T+w) \frac{1}{2\pi\sigma_\alpha\sigma_\delta} e^{\frac{-\delta^2}{2\sigma_\delta^2}} e^{\frac{(w/\delta^2)^2}{2\sigma_\alpha^2}} dw \quad (3.27)$$

Using a Dirac delta function identity to simplify our posterior, we find:

$$P(\delta|T) \propto \frac{1}{\delta^2} \frac{1}{2\pi\sigma_\alpha\sigma_\delta} e^{\frac{-\delta^2}{2\sigma_\delta^2}} e^{\frac{(-T^2/\delta^4)}{2\sigma_\alpha^2}}. \quad (3.28)$$

We've found the analytic posterior for a 1-pixel case. We can apply the same technique to a 2-pixel case and find the posterior as:

$$P(\delta_1, \delta_2|T_1, T_2) \propto \frac{1}{2\delta_1^2\pi\sigma_\alpha\sigma_\delta^2} \delta^D \left(T_2 - \frac{T_1}{\delta_1^2} \delta_2^2 \right) e^{\frac{-\delta_1^2}{2\sigma_\delta^2}} e^{\frac{-\delta_2^2}{2\sigma_\delta^2}} e^{\frac{-T_1^2}{2\delta_1^4\sigma_\alpha}}. \quad (3.29)$$

We can then marginalize over one of the δ values to obtain the analytic posterior for one density pixel:

$$P(\delta_1|T_1, T_2) \propto \frac{1}{2\delta_1^2\pi\sigma_\alpha\sigma_\delta^2} \int_{-\infty}^{\infty} \delta^D \left(T_2 - \frac{T_1}{\delta_1^2} \delta_2^2 \right) e^{\frac{-\delta_1^2}{2\sigma_\delta^2}} e^{\frac{-\delta_2^2}{2\sigma_\delta^2}} e^{\frac{-T_1^2}{2\delta_1^4\sigma_\alpha}} d\delta_2. \quad (3.30)$$

This exemplifies that solving for the analytic posterior becomes more complicated with every pixel added, and we still remain in one dimension. It should be noted that this analytic solution is a luxury that is only common for simpler problems such as the one we outline here. When we turn to solving the more complicated problem of determining the density

field in 1D or 3D during reionization, the posterior will no longer be as tractable as the 1 and 2-pixel version. We need to consider the correlation between adjacent pixels within the field and move beyond the simple quadratic toy model. This is where a Monte Carlo method comes in to sample from the posterior. We show a simple run of *emcee* for this model below.

In figure 3.3 below, we show the results of applying *emcee* on the quadratic toy model ($T = \alpha\delta^2$) for a two pixel universe. There is a degeneracy appearing in our toy model because of the squared density fluctuations. This is shown in the tadpole like appearance of our posteriors when comparing the sampled values of two parameters. For our two brightness temperatures equal to 5 and 11 mK that we chose, and taking the median value of our samples for the first pixel:

$$T_{1,actual} = 5mK \tag{3.31}$$

$$T_{1,model} \approx 4.9mK. \tag{3.32}$$

We find that *emcee* does an excellent job at correctly predicting the density field in this toy model.

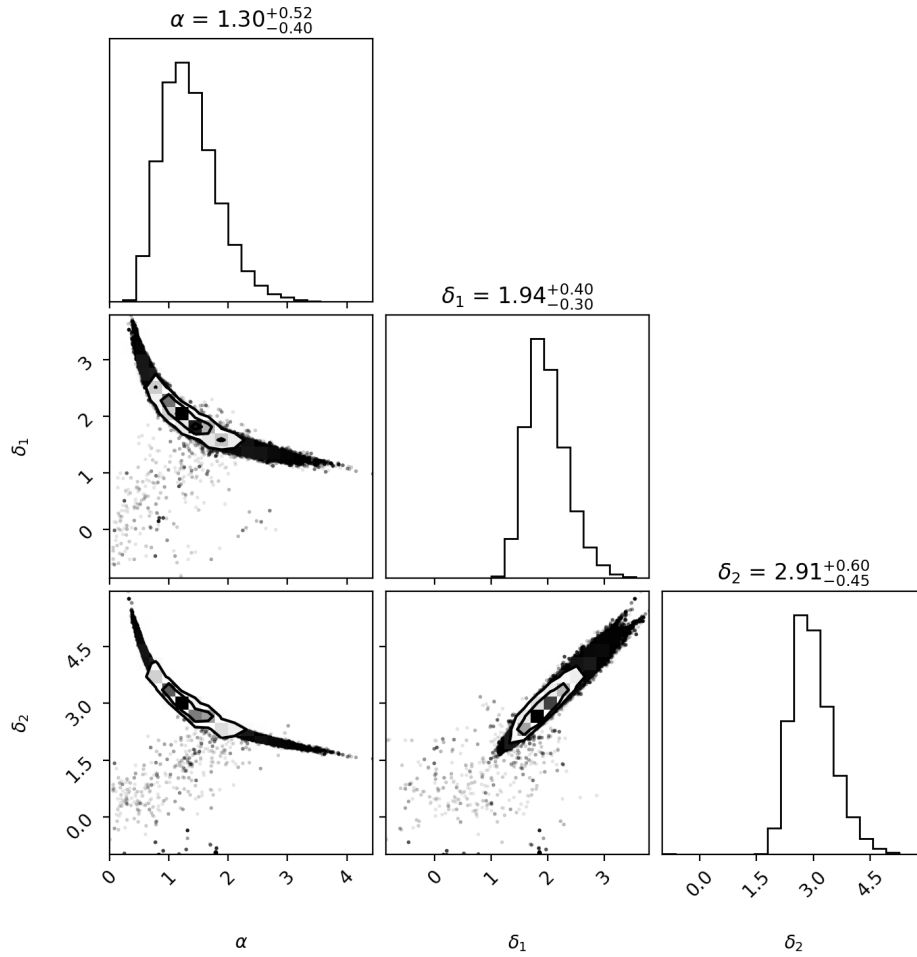


Figure 3.3: A two pixel universe application of *emcee* with our toy model. We used two brightness temperatures equal to 5 and 11 mK for the first and second pixel, respectively. Note that the α parameter is assumed to be in mK as we assume densities without units in this case.

3.5 An Analytic Likelihood Function for Density Fields

We now move to the discussion of the analytic likelihood function to replace the toy model (see equation 3.14). We begin with a model for deriving the 21-cm brightness temperature from the matter density field, $\delta_m(\mathbf{r})$ (see equation 1.6), originally derived in [5]. We then use Bayes' theorem to invert this inference. In [5], a high-resolution radiation-hydrodynamics simulation is parameterized into the analytic function we use in our likelihood. We need to switch from the toy model described previously to a realistic likelihood that describes the physics in reionization. Luckily with [5], we have the machinery to write down an analytic likelihood that we can easily sample with Monte Carlo methods. It's shown in [5] that the fluctuation fields of density and reionization redshifts are extremely correlated on scales larger than $1 \text{ Mpc } h^{-1}$ (where $h = \frac{H_0 s \text{ Mpc}}{100 \text{ km}}$). The fractional perturbation to the reionization redshift field is defined as:

$$\delta_z(\mathbf{r}) \equiv \frac{[1 + z_{RE}(\mathbf{r})] - [1 + \bar{z}]}{1 + \bar{z}}, \quad (3.33)$$

where z_{RE} is the redshift at which a pixel ionized and \bar{z} is the midpoint of reionization.

We can use the power spectra of the reionization and density field to construct a linear bias function at the midpoint redshift of reionization

$$b(k) = \sqrt{\frac{P_{zz}(k)}{P_{mm}(k)}}, \quad (3.34)$$

where $P_{mm}(k)$ is the matter (m) power spectrum and P_{zz} is the redshift of reionization power spectrum. The redshift of reionization power spectrum, P_{zz} , is the power spectrum of the fluctuation field of the average redshift of reionization, $\delta_z(\mathbf{r})$. P_{mm} is the matter power spectrum as described in equation 1.7, or the Fourier transform of two-point correlation function of density.

The linear bias function is fit to three parameters as follows:

$$b(k) = \frac{b_0}{(1 + k/k_0)^\alpha}, \quad (3.35)$$

where b_0 is the bias amplitude, k_0 is the scale threshold, and α is the asymptotic exponent. We must note that the fit is weighted by the cross-correlation of the matter and redshift power spectra to determine these parameters:

$$r_{mz}(k) = \frac{P_{mz}(k)}{\sqrt{P_{zz}(k)P_{mm}(k)}}. \quad (3.36)$$

The authors then apply a least-squares fit weighted with equation 3.36. Their best fit values of k_0 and α are displayed in table 3.5. It provides more weight on larger scale highly correlated regions than small scale correlations. b_0 is not fit in [5] because of the smaller box sizes used in their simulations. It was derived using excursion set formalism (or extended Press-Schechter formalism) and is also shown in table 3.5 below. r_{mz} and b_{mz} as a function of k are shown in 3.4 below for different RadHydro simulations.

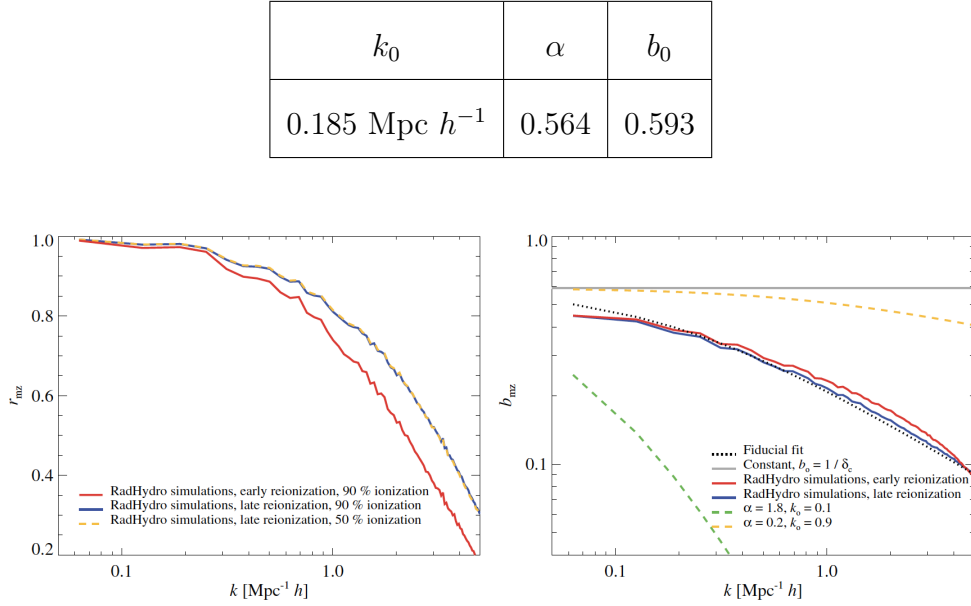


Figure 3.4: The correlation (left) and bias (right) as a function of redshift are shown for various RadHydro simulations. The orange and light green lines on the right plot show the extremes of the bias function for long and short reionization, respectively. Both plots are from [5]

Our analytic model for going from density to brightness temperature field is constructed in several steps as follows. The matter density field, $\delta_m(\mathbf{r})$, is Fourier transformed at $z = \bar{z}$, such that we have $\tilde{\delta}_m(k)$. We then multiply by the filter:

$$W_z(k) \equiv b(k)\Theta(k), \quad (3.37)$$

where $\Theta(k)$ is the Fourier transform of a top-hat filter in configuration space that smoothes out the density field to a resolution to our desired resolution, i.e., 1 Mpc h^{-1} .

With this multiplication of the filter we have $\tilde{\delta}_z(k)$:

$$\tilde{\delta}_z(k) = W_z(k)\tilde{\delta}_m(k) \quad (3.38)$$

We then inverse Fourier transform back into configuration space to find δ_z , the fluctuation in z from the midpoint of reionization at which a pixel ionizes. From δ_z , we can go back to the redshift of reionization field, $z_{RE}(\mathbf{r})$ by inverting $\delta_z(\mathbf{r})$ in equation 3.33.

We can then set the neutral hydrogen fraction within each pixel depending on if $z_{RE}(\mathbf{r})$ is greater or less than our input redshift. From there we calculate an approximate brightness temperature field from (defined originally in section 2.2):

$$\delta T_b(\nu) \approx 27 X_{HI} (1 + \delta_{nl}) mK, \quad (3.39)$$

where δ_{nl} is the non-linear matter density field.

Our final likelihood to sample from is:

$$P(\mathbf{T}|\boldsymbol{\delta}) = \frac{1}{\det(2\pi\mathbf{C})} e^{-\frac{1}{2}\Delta\mathbf{T}^T\mathbf{C}^{-1}\Delta\mathbf{T}}, \quad (3.40)$$

where $\Delta\mathbf{T} = \mathbf{T}_{measure} - \mathbf{T}_{model}(\boldsymbol{\delta})$, the difference between our measured and analytically derived brightness temperature and \mathbf{C} is the covariance matrix of deviations in our brightness temperature field. We assume a Gaussian likelihood that's a function between the difference

in measured and modeled brightness temperature, i.e., we assume Gaussian noise. In this work, we set non-diagonal entries of the covariance matrix equal to 0 as we assume that the noise is independent and not correlated between pixels.

We find the log likelihood to maintain computational efficiency as is usually used done in MCMC. This is

$$\ln(P(\mathbf{T}|\boldsymbol{\delta})) = \ln\left(\frac{1}{\det(2\pi C)}\right) - \frac{(\mathbf{T}_{\text{meas}} - \mathbf{T}_{\text{mod}})^2}{2\sigma_T^2}, \quad (3.41)$$

where σ_T is the standard deviation of the measured brightness temperature, \mathbf{T}_{meas} . This will not be derived here, but the analytic gradient of our likelihood is:

$$\frac{\partial \ln L}{\partial \delta_j} = \frac{27}{\sigma^2} \left[\left(X_j^{HI} (T_j^{\text{meas}} - T_j^{\text{mod}}) + \Sigma_a (T_a^{\text{meas}} - T_a^{\text{mod}}) (1 + \delta_a) \frac{-1}{2\Delta z_{\text{local}}} \text{sech}^2\left(\frac{z_a^{\text{re}} - z}{\Delta z_{\text{local}}}\right) (1 + \bar{z}) (\tilde{b}(|\mathbf{r}_a - \mathbf{r}_j|)) \right) \right]. \quad (3.42)$$

This analytic gradient is especially useful because of its closed form solution. We do not have to numerically differentiate to determine this gradient when we sample from an HMC. This will be a key point in our future work, and we can easily calculate the gradients as we sample the posterior.

Chapter 4

Predicting the Matter Density Field during Reionization

We have seen that post reionization, up to $z \lesssim 3$, galaxy surveys have derived matter density correlation functions or Fourier transforms of them, i.e., power spectra. As noted in chapter 2, many powerful radio instruments with primary science goals related to reionization will have their first light in the next decade. The most relevant to this work are the Hydrogen Epoch of Reionization Array (HERA) and the Square Kilometer Array (SKA) due to their drastic increase in sensitivity. By better localizing redshifted HI regions, we are better able to understand the spatial distribution of HI and HII regions during reionization. Their instrumental sensitivity will enable more accurate brightness temperature field measurements from reionization redshifts. This brightness temperature field gives us the ionization field,

and through the work in this thesis, it provides us a window into understand the density field. This is because we expect correlation in the density fields of our universe as ionized bubbles more easily ionize neighboring regions.

There is some potential for confusion between low density and ionized regions. However, it is quite unlikely that a lower density region would have a temperature brightness of zero. In addition, the spatial correlations between different pixels enable us to differentiate between low density regions and ionized bubbles. The spatial coherence properties of ionized regions and low density regions are different.

We can partially solve our problem with an initial guess for the density field given brightness temperature observations through deep learning methods, such as generative adversarial networks (GANs) or U-NETs as seen in [19]. Without error bars on these densities however, the calculated fields are less useful. As described in chapter 3, Bayesian inference presents itself as an ideal tool to derive posteriors of density fields.

In section 4.2, the major result of this work will be presented. We make progress towards constraining the density field at various redshifts with accompanying error bars and exploring the subtleties of sampling from high dimensional parameter space. We also show the calculated power spectra for the true density field, constructed density field, and a field where we set the ionized pixels to 0 in section 4.3. Section 4.4 will explore future work on density field posterior constraints. We limit our dimensionality to a 1D or line universe in this thesis. Eventually, we hope to expand this to 3D for large scale density fields but

recognize that this will most likely take hundreds of hours of supercomputing time.

The midpoint of reionization is currently constrained to $z = 7.6_{-0.7}^{+0.8}$ from [20], and this is the \bar{z} set in our model. We know that as we explore higher and lower redshifts, we expect to see varying neutral hydrogen fractions ($x_{HI} = 1 - x_{HII}$). Redshift acts as a proxy for x_{HI} . As we test our *emcee* and HMC sampler (described in section 3.2 and 3.3) for various redshifts, we change ionization fraction ($1 - X_{HI}$) of our brightness temperature fields between 0 and 1. This allows the exploration of a variety of ionized fractions which is key in determining the robustness of our derived posteriors.

We do not use evolving density fields as we decrease in redshift but generate log normal correlated fields using a non-diagonal covariance matrix and Cholesky decomposition. This is unrealistic. We expect denser regions to grow denser through gravity as the universe matures, and reionization to happen sooner in overdense regions as a result of the higher number of ionizing sources. As our aim is to explore the potential of this method for determining density field measurements, we neglect the changing density field in our current iteration.

4.1 Initial Attempt with *emcee*

We initially tried sampling our posterior with *emcee*. This worked well for small dimensionality, low ionization, and when we start our MCMC walkers close to their actual value. See figures 4.1 and 4.2 for an example of how well this method works when we start our walkers slightly perturbed from the actual density values. The perturbations are pulled

from a normal distribution with standard deviation of 1. Some walkers were started slightly above and others below the actual density values. In these figures, we show the true input density values and 100 samples from the MCMC chain. We also show the pixels that are ionized in yellow. The turquoise bands around the truth densities show the rough error we could expect with this method.

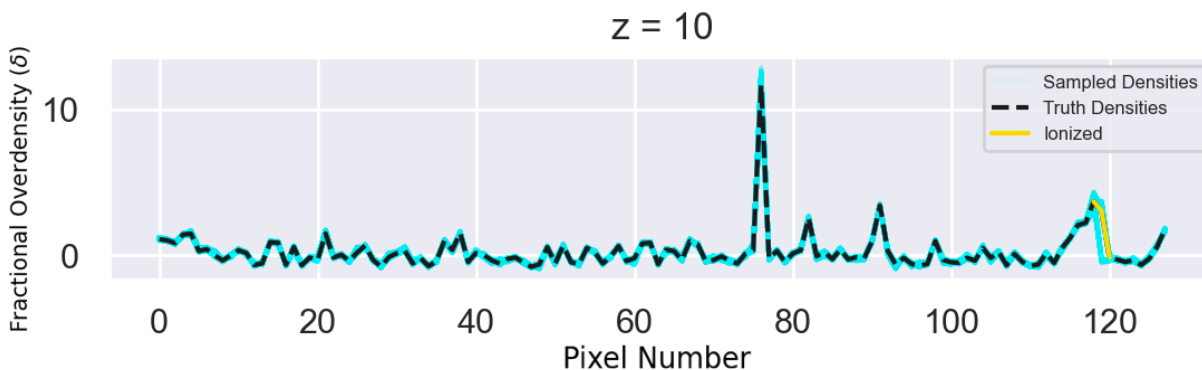


Figure 4.1: Overview of 1D density field at redshift = 10 for *emcee*. The black dashed line is the actual matter density field. The yellow regions are the ionized regions of the density field. Walkers are started very close to their actual values which leads to convergence to the actual density field. The span of the turquoise points here represent a pseudo-error bar that is an underestimate.

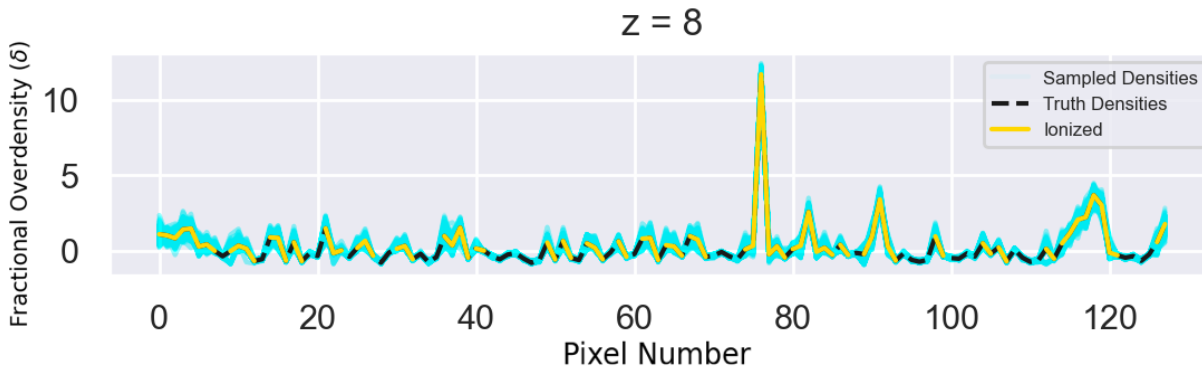


Figure 4.2: The same plot as 4.1 but for redshift = 8.

When starting the walkers randomly for a temperature brightness field in a completely neutral universe at $z = 15$, we saw a drastic decrease in performance. We can consider figure 4.3 below for an example of this. We would expect this universe without ionization to be the simplest case for our sampler and a similar result to what we see in figure 4.2 and 4.1. We run *emcee* for approximately 100,000 samples with around 256 walkers and still do not see significant convergence. Due to the inefficiency of *emcee* when sampling many parameters, even the simplest of cases fails to perform well. We pick this simple case because we can easily estimate the errors on the density field. We expect an error in the density field of a neutral universe to be approximately equal to $\sigma_T/27 = 0.03$ (derived from equation 2.12), where $\sigma_T = 1$. This extremely slow convergence is typical for sampling higher dimensions using *emcee*, and we need to switch methods. This made it essential to switch to an HMC to produce accurate results.

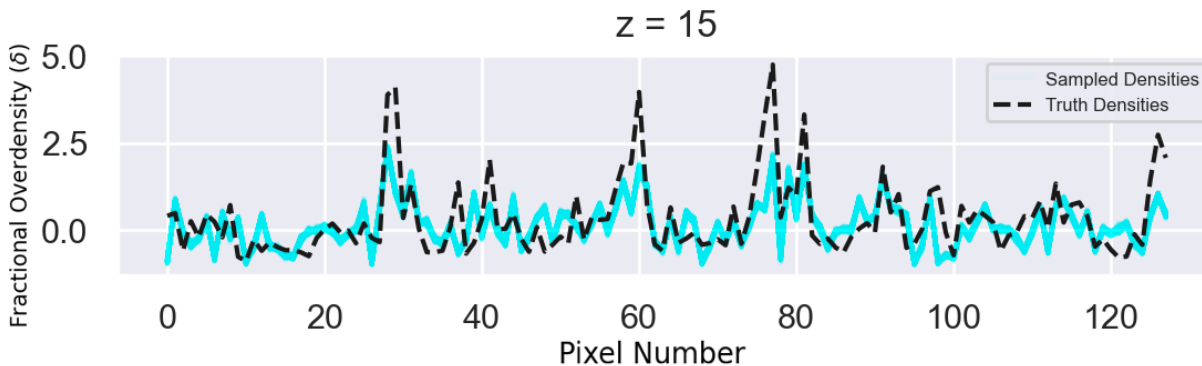


Figure 4.3: A similar plot to 4.1 where walkers are initialized completely randomly in a neutral universe at redshift = 15.

4.2 Density Error Estimates with HMC

We begin our exploration with HMC for a completely neutral universe which is our simplest case. Our initial results for a completely neutral universe as seen in figure 4.3. In this figure, we again overlay the samples onto the truth densities to compare. We immediately see better results for a 2000 samples case with HMC. We note that there is more than 2000 samples taken with the HMC, but the NUTS sampler throws out 1000s of other samples in between. The last 1000 samples in turquoise out of 2000 total samples from our posterior are seen around the truth densities.

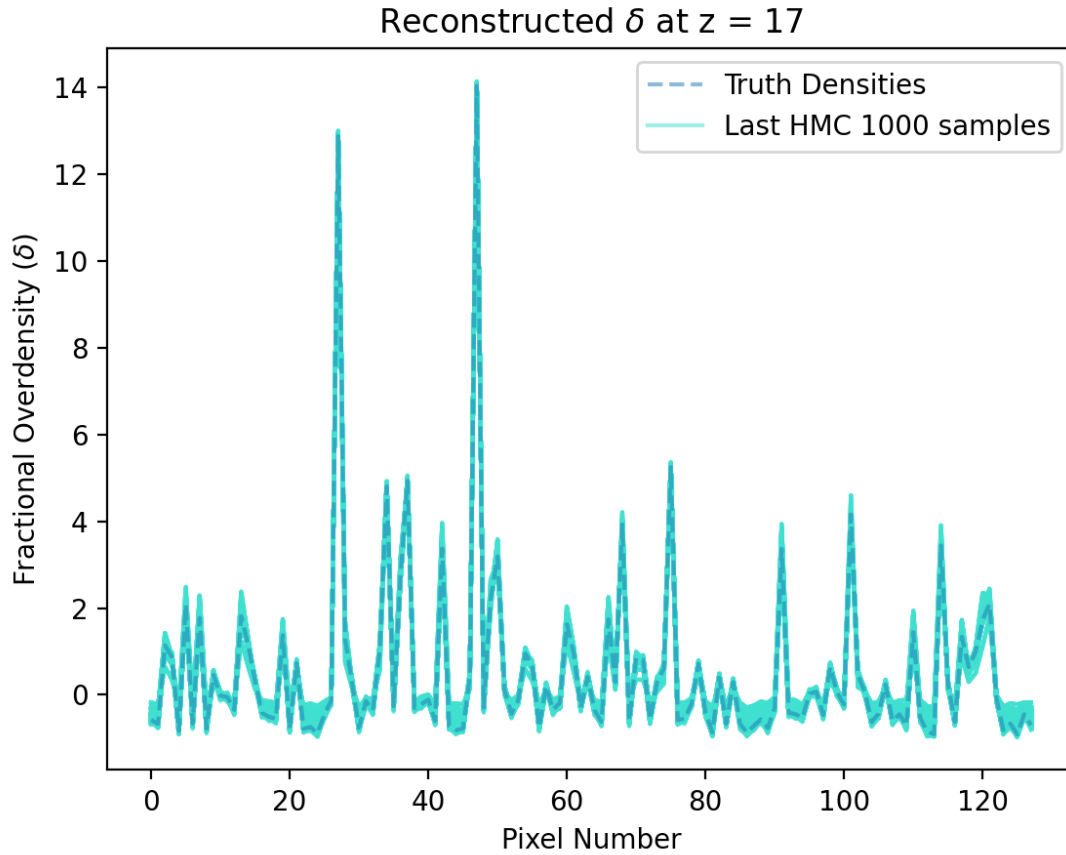


Figure 4.4: A completely neutral universe’s density field at redshift = 17 predicted the HMC. The turquoise band around the truth densities again represents the rough errors of the predicted densities. Compared to figure 4.3, the HMC walkers converge easily.

As we introduce some ionization, the HMC quickly shows computational inefficiency. We can see the effects of decreasing our redshift and thus increasing ionization fraction in in figure 4.5. The increase in ionization can be seen by the three yellow ionized pixels. Now, there are three ionized pixels compared to redshift = 17 as seen in 4.4.

All pixels are started randomly again in this plot except those that are ionized. The

ionized pixels are started perturbed from their actual values. As in the previous section, the perturbations are drawn from a normal distribution with standard deviation equal to 1. We choose to only perturb the ionized regions because we know these are the most difficult regions to sample. They will have a temperature brightness equal to 0 and rely on correlations within the likelihood to converge to the correct density. This also allows the HMC to explore the probability region around the actual value rather than going directly to -1. The easiest solution for the sampler for an ionized pixel is to go to a density of -1. This was motivated by our tests when we started the ionized regions at 0, and they tended to go to -1 and failed to sample higher and more accurate densities.

After the same number of samples, we don't see nearly as much convergence as we saw in 4.4. Looking at $z=17$ and $z=12$, we see that an increase in pixel number and ionized pixels for the same number of samples drastically decreases the number of samples in the vicinity of the actual densities.

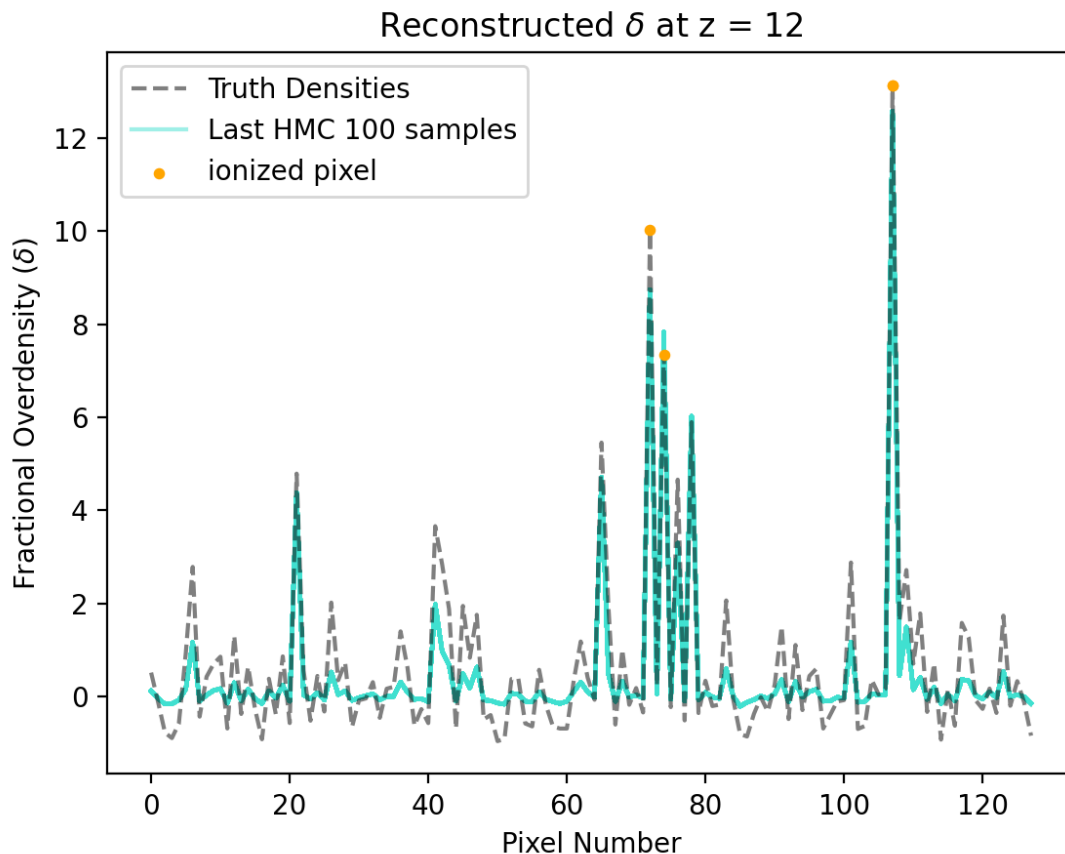


Figure 4.5: A universe’s density field with three ionized pixels seen in yellow at redshift = 12 predicted by the HMC. Compared to figure 4.4 which was sampled the same amount, the HMC walkers no longer converge to the proper densities.

The combination of increased pixel number and increased ionization fraction leads to a difficult sampling problem. To decrease computational time, we instead explore a similar universe to that seen in figure 4.5 with only 32 pixels. This is seen in figure 4.6. Here, all pixels converge to the proper density value. With an ionized pixel, we also need to increase the standard deviation of the Gaussian prior from 1 to 4. This is to ensure that the prior

doesn't pull the ionized pixel densities down to -1 as we saw occurring during tests despite starting the sampler near the actual density. Figure 4.7 shows the difference in actual and sampled density fields. The error between the two is concentrated around the ionized pixel as expected.

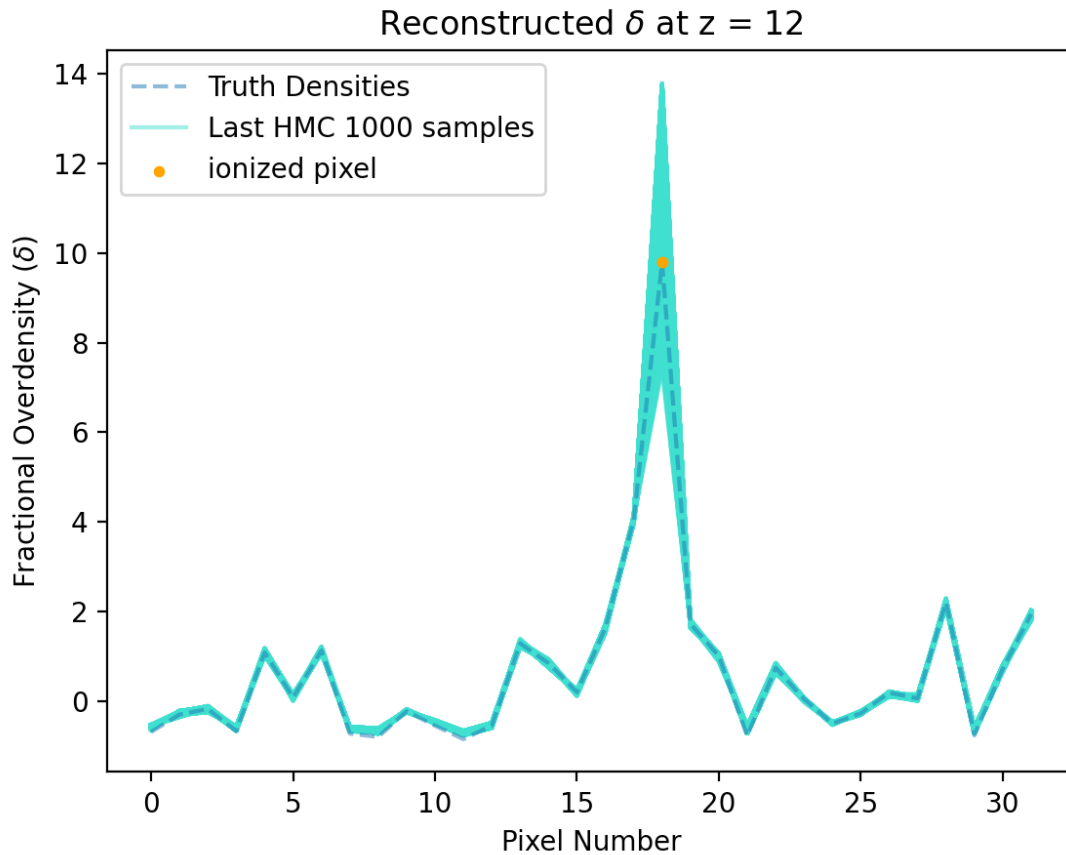


Figure 4.6: Similar to figure 4.5 but at 32 pixels. We show the last 1000 samples.

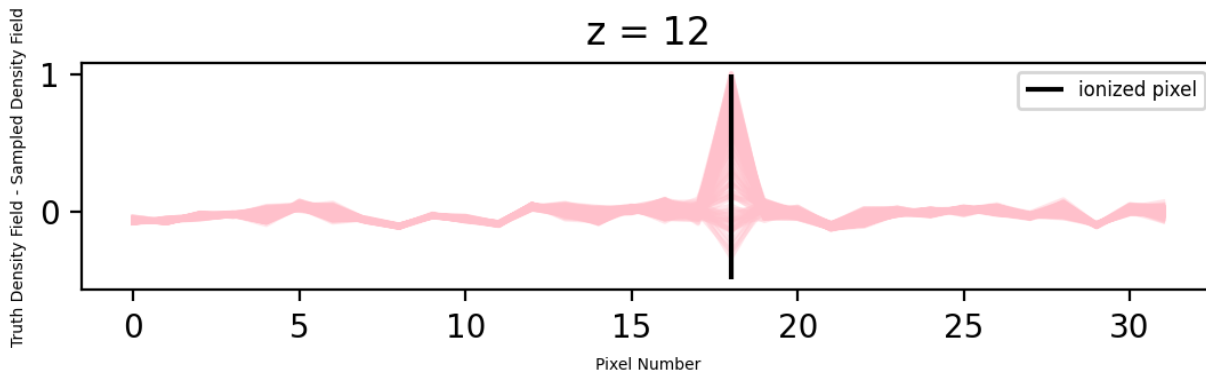


Figure 4.7: The difference between the actual density field and sampled density fields are shown in this plot for the last 100 samples are shown in this plot.

Although, we see great performance for one ionized pixel in a 32 pixel universe, we still need to incorporate more optimal sampling techniques that are better at sampling multimodal posteriors to constrain the density field more precisely. The errors around the ionized pixels are larger than the neutral density pixels as expected.

4.3 Comparing Theoretical and Predicted Power Spectra

Lastly, we derive power spectra considering all ionized pixels are turned off ($P_{ionized=0}$) (or set to 0), the theoretical power spectrum (P_{true}), and the power spectrum calculated with our sampler ($P_{constructed}$). We note that $P_{ionized}$ is really just making the very naive assumption that the density field and brightness temperature field are equal to each other.

Our $P_{constructed}$, takes the last 1000 samples of the density field to construct 1000 power spectra. At a higher redshift with no ionization, we see the best results. The power spectra constructed lie close to the actual true power spectrum for high redshifts. $P_{ionized=0}$ does significantly worse and does not track the shape nor amplitude of the true power spectrum for both $z = 17$ and $z = 12$. The purple bands correspond to the errors of the predicted power spectra compared to the true power spectrum.

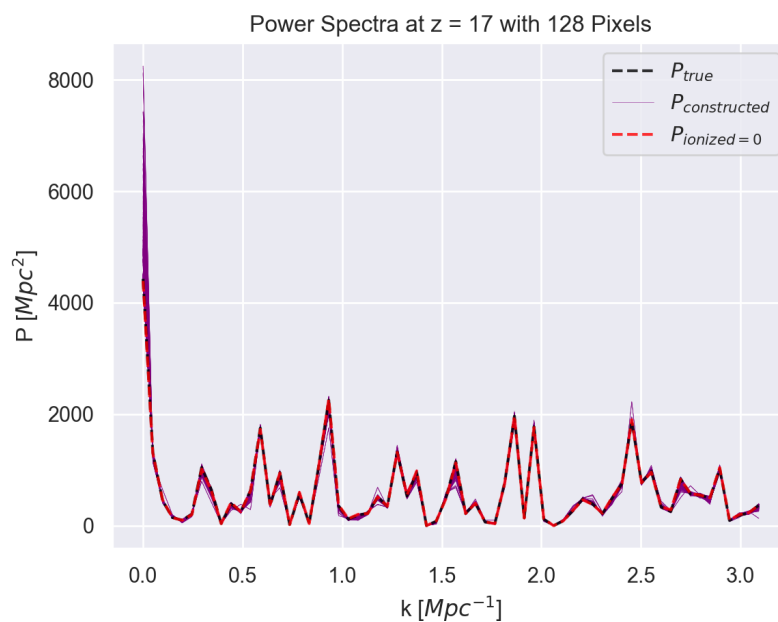


Figure 4.8: Corresponding to figure 4.4 spectra for the 1000 last samples ($P_{constructed}$), the true density field (P_{true}), and the power spectra we determine if we set all ionized pixels to 0 ($P_{ionized}$). The $P_{ionized}$ spectrum is the same as P_{true} since at redshift = 17, they're completely neutral.

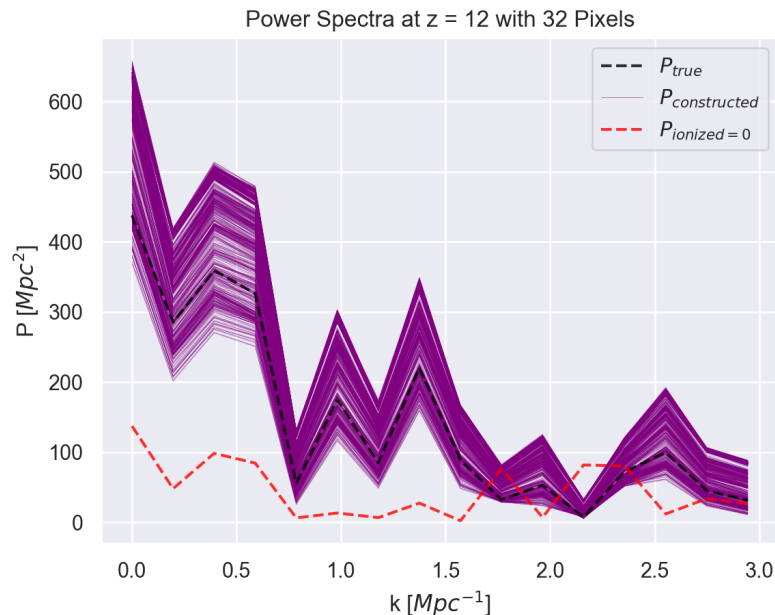


Figure 4.9: Similar to figure 4.8 but at redshift = 12 corresponding to the predicted density field in figure 4.6. The errors in the power spectra are notable here compared to redshift = 17.

Our constructed power spectra deteriorate as we go to lower redshifts. We see that the spread of both the samples and power spectra gets wider as we go to lower redshifts. For an ionized pixel, we have zero information coming from the temperature brightness so we have to rely on correlations with the neutral density field. The deterioration of performance makes sense in this context. However, we see that $P_{ionized}$ does very poorly compared to $P_{constructed}$ at $z=12$. The purple power spectra follow the true power spectrum closely.

4.4 Future Large Scale 3D Density Field Posteriors

While significantly more technical issues need to be surpassed to make a density field reconstruction work for real observations, we have shown that this reconstruction could be possible. This may further aid in our understanding of large scale structure and its evolution during reionization. The work in this thesis takes a lower dimension approach to reconstructing the matter density. We assume an analytic correlated density field rather than extracting the field from the semi-analytic simulations found in 21cmFAST. This leads to a static density field throughout the evolution of the universe which is not physical. By using a more accurate changing density field, we expect to be able to more realistically test this framework. Our 1D universe is useful for proof of concept of our model but is also inaccurate. We need to test our model with more accurate density fields in 3D. When going to a 3D density cube, we are consequentially sampling $128^3 \approx 2e6$ densities if our cubes are 128 pixels one each side. This is a regime where *emcee* no longer serves useful, and HMC requires many supercomputer hours to provide meaningful results. As HERA comes online, we will be able to place well localized constraints on the brightness temperature field of our universe probing redshifts between 6-13.

We showed that we do need to be careful about where we set our initial conditions due to multimodal distributions within the density field posterior. We may be able to get a closer estimate to the density field by using a maximum-a-posteriori (MAP) estimate as described in [21]. However, this is saved for future work. There is a significant amount of information

in the temperature brightness field that can be used to understand the density field, but sampling can be very tricky and requires significant future work.

Chapter 5

The Ionosphere and Low-Frequency

Radio Astronomy

The ionosphere mostly lies in space according to the Karman line (above 100 km), i.e., a definition for the line separating outer space and Earth's atmosphere. The International Space Station orbits *within* the ionosphere at about 410 km. Carl Friedrich Gauss (of Gauss's Law in electricity and magnetism) was the first to speculate that the higher parts of the atmosphere might contain an ionized region. It was not until 1924 when physicists, Edward Appleton and Miles Barnett, proved the existence of an ionosphere by reflecting radio waves off the atmosphere [22].

The Earth's atmosphere can become a huge barrier to detecting radiation on Earth. The atmosphere is opaque to much of the electromagnetic spectrum, but there is a sweet spot

for certain wavelengths of radio waves where the opacity is much lower. Nevertheless, low frequency radio astronomy is limited by the ionized medium that makes up the ionosphere. The Earth's ionosphere reflects wavelengths below $\nu \lesssim 10\text{MHz}$ or above $\lambda \gtrsim 30\text{m}$, derived in section 5.1 below. The ionosphere completely blocks the lowest frequencies from reaching Earth and distorts higher frequency radiation that does pass through it. As radio astronomy probes lower and lower frequencies on Earth, an understanding of the effects of the ionosphere is increasingly important to make higher precision measurements.

The Earth's atmosphere is partially ionized between about 60 to 1000 km above the surface. The ionosphere is characterized as a weak plasma (due to its partial ionization) and has effects on radiation similar to a plasma. The ionosphere is ionized by cosmic and solar radiation through UV, X-rays and a constant stream of plasma. The electrons then behave as free electrons in the upper atmosphere. More specifically, the very hot corona of the sun emits both UV and X-rays as well as a constant stream of plasma that leads to this ionization. Only about 1 % of the atoms in the ionosphere are ionized. Maximum ionization occurs around 300 km where there are about 10^{10} to 10^{13} free electrons per cubic meter [23].

At night, solar photoionization no longer contributes to the ionization, but charged particles from the sun and elsewhere still do. These cosmic rays can originate from supernovae, black holes, neutron stars, etc., and are a large area of study on their own. The magnetosphere is the area around the Earth where charged particles are affected by the Earth's magnetic field. It also plays a role in ionization as it redirects charged particles

along the Earth's magnetic field lines. The magnetic field is approximately dipolar such that it redirects cosmic rays to the magnetic poles which lie near the North and South geographic poles.

5.1 Plasma Frequency Derivation

We now calculate the impact of free electrons on radiation, i.e., the plasma frequency. The plasma frequency itself is the oscillation frequency as the material falls back into electrical equilibrium. The ionosphere is a plasma which when perturbed oscillates at the plasma frequency. Below this frequency electrons have enough time to respond and equilibrate, blocking the wave. Above the plasma frequency however, the electrons are unable to fully cancel out the radiation and we are able to see the signal at our telescopes on Earth. The approximate plasma frequency of the ionosphere is on the order of 10MHz. As we reach lower frequencies and higher wavelengths to probe different science, the ionosphere becomes a larger problem.

Using [24] as a reference for this derivation, we can derive the plasma frequency for a plane wave entering a plasma. We can take a simplification and model a plasma in the ionosphere as a damped simple harmonic oscillator (DSHO) where the electrons act as little springs making up the corners of the lattice.

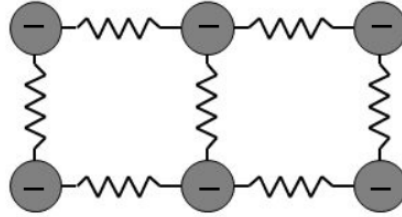


Figure 5.1: Distilled model of free electrons in ionosphere in a simple lattice structure. Modified Image Credit: Ilene Dixon

The wave propagates through the ionosphere, and a separation between positive and negative charges is created. Briefly, the electrons will be displaced slightly and move back towards the positive charge. They go too far and then reverse back the way they came, creating an approximate DSHO. The harmonic motion takes place at the plasma frequency as derived below.

We consider a plane wave incident on the DSHO described by the usual E and B fields:

$$\vec{B} = B_0 e^{i(\mathbf{k}\cdot\mathbf{r}-\omega t)} \quad (5.1)$$

$$\vec{E} = E_0 e^{i(\mathbf{k}\cdot\mathbf{r}-\omega t)} \quad (5.2)$$

Now, all the forces acting on the electrons in this "lattice" are as follows:

$$\vec{F}_{electric} = -e\vec{E} \quad (5.3)$$

$$\vec{F}_{magnetic} = -e\frac{\vec{v}}{c} \times \vec{B} \quad (5.4)$$

$$\vec{F}_{spring} = -k\vec{x} \quad (5.5)$$

$$\vec{F}_{drag} = -\gamma\vec{v}, \quad (5.6)$$

where we add on some approximate linear drag force, e is the charge of an electron, \vec{v} is the velocity of an electron, k is the spring constant, and γ is some drag constant.

We can replace our spring constant, k , using the characteristic frequency:

$$\omega_0 = \sqrt{\frac{k}{m_e}} \quad (5.7)$$

$$k = \omega_0^2 m_e \quad (5.8)$$

Simply using Newtonian mechanics, we can equate the mass times acceleration to the sum of these forces:

$$m\ddot{\vec{x}} = -e\vec{E} - e\frac{\vec{v}}{c} \times \vec{B} + \omega_0^2 m_e \vec{x} - \gamma\vec{v} \quad (5.9)$$

We can drop the magnetic force term as we assume that the E-field will dominate in this case. This approximation works because the electrons are not moving at relativistic speeds so we expect the B-field to be small. We also ignore the Earth's magnetic field which causes

a gyrofrequency for electrons of roughly 1MHz making it relatively negligible.

$$m\ddot{\vec{x}} = -e\vec{E} - \gamma\dot{\vec{x}} + \omega_0^2 m_e \vec{x} \quad (5.10)$$

$$x = \frac{-e}{m_e} \frac{(\omega_0^2 - \omega^2) + i\omega\gamma}{(\omega_0^2 - \omega^2)^2 + (\omega\gamma)^2} E_0. \quad (5.11)$$

Let's simplify even further and ignore any drag force, i.e., $\gamma = 0$,

$$x = \frac{-e}{m_e} \frac{(\omega_0^2 - \omega^2)}{(\omega_0^2 - \omega^2)^2} E_0 \quad (5.12)$$

$$x = \frac{-e}{m_e} \frac{1}{(\omega_0^2 - \omega^2)} E_0. \quad (5.13)$$

Now, we examine the current density:

$$\vec{J} = -ne\dot{\vec{x}} \quad (5.14)$$

Replacing \dot{x} with the derivative of x :

$$\vec{J} = \frac{-ne(-i\omega)(-eE_0)}{m_e(\omega_0^2 - \omega^2)} \quad (5.15)$$

$$\vec{J} = \frac{-ne^2(-i\omega)(E_0)}{m_e(\omega_0^2 - \omega^2)} \quad (5.16)$$

Relating the current density to the conductivity:

$$\vec{J} = -\sigma\vec{E} = \frac{-ne^2(-i\omega)(E_0)}{m_e(\omega_0^2 - \omega^2)} \quad (5.17)$$

$$\sigma = \frac{ne^2(-i\omega)}{m_e(\omega_0^2 - \omega^2)} \quad (5.18)$$

Maxwell's Equations in CGS units are now needed to continue this derivation, where the last part of the equations are from the incident plane wave and its corresponding wave vector, \vec{k} :

$$\nabla \times \vec{E} = -\frac{1}{c} \frac{\partial \vec{B}}{\partial t} = i\vec{k} \times \vec{E} \quad (5.19)$$

$$\nabla \times \vec{B} = \frac{4\pi}{c} \vec{J} + \frac{1}{c} \frac{\partial \vec{E}}{\partial t} = i\vec{k} \times \vec{B} \quad (5.20)$$

We further find that:

$$i\vec{k} \times \vec{E} = \frac{i\omega\vec{B}}{c} \quad (5.21)$$

$$i\vec{k} \times \vec{B} = \left(\frac{4\pi\sigma}{c} - \frac{i\omega}{c} \right) \vec{E} \quad (5.22)$$

Combining these two equations:

$$i\vec{k} \times \left(\frac{c}{i\omega} i\vec{k} \times \vec{E} \right) = \left(\frac{4\pi\sigma}{c} - \frac{i\omega}{c} \right) \vec{E} \quad (5.23)$$

$$(-ik)^2 \frac{c}{i\omega} = \left(\frac{4\pi \frac{ne^2(-i\omega)}{m_e(\omega_0^2 - \omega^2)}}{c} - \frac{i\omega}{c} \right) \quad (5.24)$$

We extract ω_p , the plasma frequency, and we assume that the characteristic frequency is close to 0 since we are exploring a diffuse plasma (the ionosphere). The plasma frequency is then:

$$\omega_p^2 \equiv \frac{4\pi n_e e^2}{m_e}. \quad (5.25)$$

Now that we've derived the plasma frequency, let's calculate what the expected plasma frequency would be for the ionosphere in the maximally ionized region where $n_e = 10^{13} e^-/\text{m}^3$ in Centimetre-gram-second (CGS) units.

$$\omega_p^2 \equiv 4\pi \frac{(10^7 e^-/\text{cm}^3)(4.80 \times 10^{-10} C)^2}{9.11 \times 10^{-28} g} \quad (5.26)$$

$$f_p \approx 20 \text{MHz}. \quad (5.27)$$

This makes sense since frequencies less than 20 MHz are distorted heavily when they arrive at our telescopes on Earth. We would have to move instruments to outer space to avoid this issue!

5.2 Ionospheric Differentiation and Formation

The ionosphere is labelled by three regions from higher to lower: F, E and D-region. At night the ionosphere consists only of the F and E layers where many of the electrons recombine with ions and neutrality is increased. During the day the ionosphere is more highly ionized by the sun and the D region is present and the highest region F is split into two regions.

The lowest layer, the D layer, is caused by ionization of nitric oxide within this layer by Lyman- α emission from hydrogen. Increased solar activity can also generate powerful X-rays that ionize N_2 and O_2 in this layer. The middle layer, the E layer, contains molecular hydrogen ionized by lower power X-rays and UV solar radiation. Lastly, the highest layer, the F layer, has the highest electron density. Ionization here is mostly due to highly energetic UV radiation that ionizes atomic hydrogen.

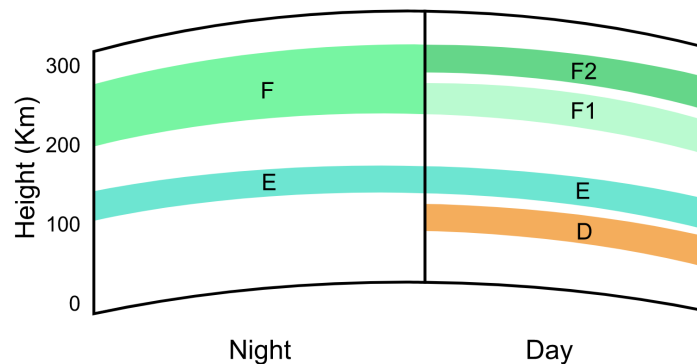


Figure 5.2: Schematic of the layers of the ionosphere. Credit: Naval Postgraduate School

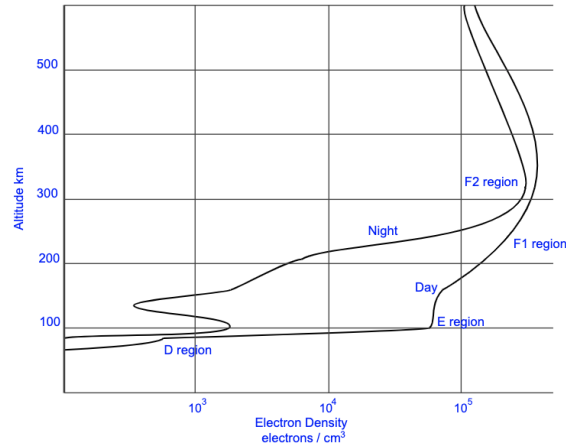


Figure 5.3: Altitude versus electron density within the ionosphere. Credit: Electronic Notes

The highest regions in the ionosphere, E and F, are responsible for reflections (or refractions that end up causing the radio wave to come back down to the surface of the Earth) of radio waves that cause them to be able to travel long distances around the Earth without an intermediate transmitter, enabling Skywave propagation (discussed in section 5.3.2).

In the D and E regions, attenuation of radio frequencies is especially prominent. As the radio waves propagate through the plasma, they vibrate free electrons with cause collisions with molecules and cause a loss of energy. This attenuation is larger for lower frequencies; the wavelength of the light is larger and so is the wavelength of the vibration, increasing the number of collisions between free electrons and molecules [25].

5.3 The Ionosphere and Radio Astronomy

Because radio waves are the longest wavelengths on the electromagnetic spectrum, they require larger instruments to detect them. For single dish radio astronomy, the ionosphere is relatively uniform above the dish, but this is still extremely dependent on observing frequency and dish size. In radio interferometry where multiple antennas are used to make precise localization measurements of sources, the effect is greatly increased. This will be described more explicitly in the subsequent subsections ranging from first to second order effects in order of decreasing importance and effect on radio astronomy. Using known precisely localized pulsars as calibrators or other techniques, the ionospheric effects can sometimes be lessened. Mitigating these effects will be discussed briefly in section ??.

5.3.1 First Order Effects

For low frequency radio astronomy instruments, e.g., the Murchison Widefield Array (MWA) or the Canadian Hydrogen Intensity Mapping Experiment (CHIME) described in [26] and [27], respectively, the ionospheric disturbances to radiation become more intense. At zenith around the the instrument, the opacity is lowest where the maximum frequency blocked by the ionosphere is around that of the plasma frequency as calculated in section 5.1. The effects increase as the elevation of the source increases as more atmosphere is passed through the farther away from the zenith observed.

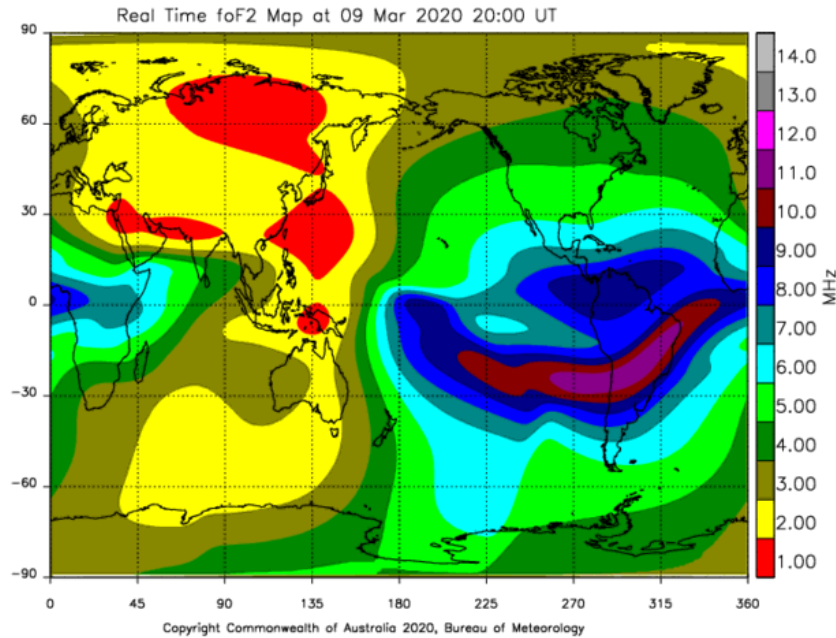


Figure 5.4: Recent map showing the plasma (critical) frequency dependence on longitude. Frequencies below the plasma frequency will be reflected back to Earth from the ionosphere. These types of maps can be created with ionosondes, which sends various frequency pulses between about 1-22 MHz to quantify which frequencies are reflected or delayed. Credit: Australian Bureau of Meteorology

5.3.2 Second Order Effects

Even during times of quiet activity within the ionosphere, these second order effects are always present. We can derive the dispersion relationship inside the plasma using 5.18 and 5.22, but the algebra is avoided here. For a diffuse plasma, ω_0 goes to values that are small compared to the CHIME observing range, and we ignore it here.

Our dispersion relation for an electron plasma is:

$$\left(\frac{kc}{\omega}\right)^2 = 1 - \frac{\omega_p^2}{\omega^2}. \quad (5.28)$$

To relate this to the index of refraction, η , we use the definition:

$$\eta \equiv \frac{kc}{\omega}. \quad (5.29)$$

$$\eta^2 = 1 - \frac{\omega_p^2}{\omega^2}. \quad (5.30)$$

We can calculate the group velocity, v_g , of a signal with:

$$v_g = \eta c. \quad (5.31)$$

We Taylor expand η for the case when frequencies observed are much greater than the plasma frequency such that:

$$\eta = \sqrt{1 - \frac{\omega_p^2}{\omega^2}} \approx 1 - \frac{1}{2} \left(\frac{\omega_p}{\omega}\right)^2. \quad (5.32)$$

The group velocity is then:

$$v_g = c \left(1 - \frac{1}{2} \left(\frac{\omega_p}{\omega} \right)^2 \right). \quad (5.33)$$

The group velocity will become more important later when we calculate the actual time delay to the ionosphere. We need the group velocity in this case, and we will integrate along the electron number density, n_e .

The closer the radio frequency to the plasma frequency of $\approx 20MHz$ the more it is refracted within the ionosphere. This can easily be seen from the relationship for the index of refraction. The larger the incident frequency, ω , is compared to ω_p , the closer to $\eta = 1$ (index of refraction is 1 in vacuum). As the index of refraction is less than one in the ionosphere, the propagating light is refracted away from the normal. This allows the so-called "Skywave" propagation ([28]) which permits frequencies around and below the plasma frequency to reflect back from the ionosphere to the Earth when released by a radio station or other radio transmitter. This can allow radio transmission at large distances without an intermediary. See figure 5.5 below for a schematic of this process.

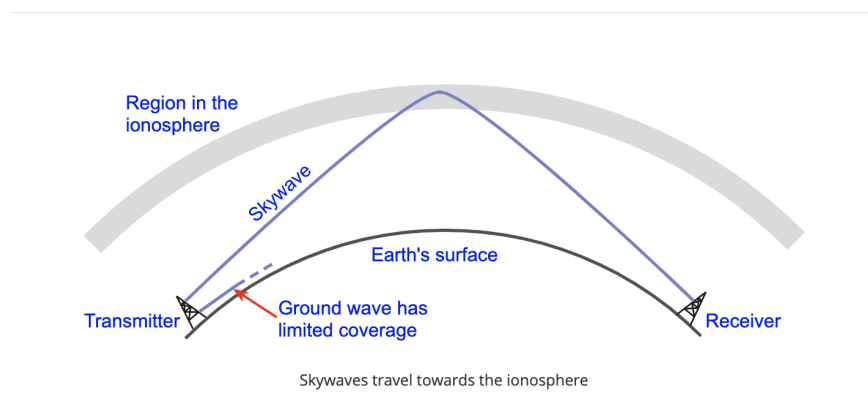


Figure 5.5: Skywave propagation can utilize the ionospheric index of refraction being less than 1 for frequencies closer to the plasma frequency to allow radio communication over large distances. Credit: Electronic Notes

In figure 5.6, the frequency dependent effects are described graphically. For frequencies close to the plasma frequency (lower radio frequencies greater than 10MHz), the refraction effect is larger. For frequencies much greater than the plasma frequency, waves propagate through the ionosphere less affected. At frequencies less than or equal to the plasma frequency, waves are reflected.

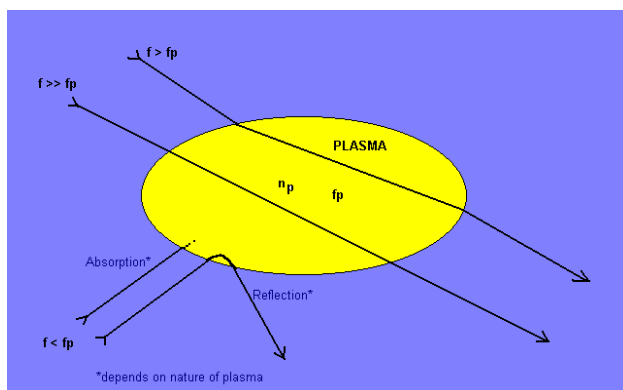


Figure 5.6: Ray diagram showing frequency dependence of waves propagating through plasma in the ionosphere where f_p and n_p are the plasma frequency and plasma number density, respectively. Credit: Australian Space Academy

The inhomogeneity of the ionosphere is especially problematic for very long baseline interferometry (VLBI) where each dish observes a very different part of the ionosphere. This is due to the varying indices of refraction as waves propagate through the medium and causes a time delay in the signal received by each interferometric element. Since VLBI measurements rely almost entirely on time delays between dishes to localize objects, this effect greatly disturbs the precision of the localization measurement.

Faraday rotation is another important second order effect within the ionospheric plasma caused not only because of the free electrons but also because of the influence of the Earth's magnetic field. It's caused by the interaction of the propagating light and the surrounding magnetic field caused by the free electrons within the plasma and the Earth's magnetic field. Faraday rotation causes a change in the polarization of the angle of the radiation, $\Delta\theta$:

$$\Delta\theta = \text{RM}\lambda^2, \quad (5.34)$$

where the rotation measure (RM) is defined by the following integral:

$$\text{RM} = \frac{e^3}{2\pi m_e^2 c^4} \int_0^d n_e(r) B_{\parallel}(r) dr, \quad (5.35)$$

where B_{\parallel} is the magnetic field strength in our line of sight.

As can be seen from the equations describing Faraday rotation, the polarization angle change is highly dependent on wavelength. Larger wavelengths or lower frequencies will

have a correspondingly larger angle change when propagating through the same plasma as smaller wavelengths. For example at 100 MHz, the effect of Faraday rotation will cause approximately three full rotations in the polarization of incident light [29].

Our dispersion relationship above is also important in that it will cause time delays in different frequencies of light travelling through the ionosphere. This can be seen by the group velocity rewritten here for convenience:

$$v_g = c \left(1 - \frac{1}{2} \left(\frac{\omega_p}{\omega} \right)^2 \right). \quad (5.36)$$

We also recall the plasma frequency as:

$$\omega_p^2 \equiv \frac{4\pi n_e e^2}{m_e}. \quad (5.37)$$

We get the time delay by taking the difference in between the actual delayed time it takes a signal to reach us and the ideal case (d/c).

$$\Delta t = \int_0^{\text{distance}} \frac{dl}{v_g} - \frac{d}{c}. \quad (5.38)$$

We integrate along the line of sight because we know the electron density is not uniform.

$$\Delta t = \int_0^{\text{distance}} \frac{dl}{v_g} - \frac{d}{c}. \quad (5.39)$$

$$\Delta t = \int_0^{\text{distance}} \frac{dl}{c \left(1 - \frac{1}{2} \left(\frac{w_p}{w} \right)^2 \right)} - \frac{d}{c}. \quad (5.40)$$

We Taylor expand to simplify the integral to:

$$\Delta t = \frac{1}{c} \int_0^{\text{distance}} 1 + \frac{1}{2} \left(\frac{w_p}{w} \right)^2 dl - \frac{d}{c}. \quad (5.41)$$

$$\Delta t = \frac{1}{c} \int_0^{\text{distance}} \frac{1}{2} \left(\frac{w_p}{w} \right)^2 dl. \quad (5.42)$$

Replacing the plasma frequency:

$$\Delta t = \frac{1}{c} \int_0^{\text{distance}} \frac{2\pi n_e e^2}{w^2 m_e} dl. \quad (5.43)$$

We note that this now shows the dispersion measure relationship of:

$$\text{DM} = \int_0^d n_e dl. \quad (5.44)$$

Typically, astronomers use pc/cm^3 as the unit for dispersion measure. The ionosphere is usually quantified in terms of a total electron content unit (TECu) or $10^6 e/m^2$. We note that $1 \text{ TECu} = 3.241 \times 10^{-7} pc/cm^3$. The range of typical vertical TEC values (or column densities) in the ionosphere can range from only a few to hundreds of TECu.

Simplifying from above and pulling constant quantities along the line of sight out of the integral:

$$\Delta t = \frac{2\pi e^2}{m_e c \omega^2} \int_0^d n_e dl = \frac{2\pi e^2}{m_e c \omega^2} DM \quad (5.45)$$

$$\Delta t = 4140 \left(\frac{DM}{pc - \text{cm}^{-3}} \right) \left(\frac{1MHz}{\nu} \right)^2 \quad (5.46)$$

$$\Delta t = 1.3 \times 10^{-3} \left(\frac{DM}{TECU} \right) \left(\frac{1MHz}{\nu} \right)^2 \quad (5.47)$$

For larger frequencies, it's evident that a smaller time delay will occur. Radio interferometers that explore lower frequency ranges, closer to the plasma frequency of the ionosphere, are especially vulnerable to time delay error. Because interferometry relies on these time delays to create images, the time delay has to be calibrated for in some way to avoid errors. At about 100 MHz (a frequency that the MWA probes), the delay is about 1.5 μs [29]. This is roughly the light crossing time of the MWA, which has baselines reaching 6 km.

Chapter 6

Pulsars as Calibrators

Before diving into GNSS satellites as calibrators, we must first examine the expected calibration technique for low frequency VLBI – using pulsars as calibrators. We hope to provide a complete catalog of all pulsars discovered that are bright and localized well enough to be used as phase calibrators. Due to the strict constraints of the needed pulsar population, the possibility of having enough suitable pulsar phase calibrators was not immediately clear.

The CHIME Outrigger sites at Allenby, Hat Creek, and Greenbank Radio Observatory (GBO) have baselines of at most 3300 kilometers from the original CHIME site at the Dominion Radio Astrophysical Observatory (DRAO). CHIME employs four 20 x 100 m cylindrical reflectors with orientations from north to south. Each reflector has 256 dual-polarization feeds and observes the northern hemisphere daily through drift-scan. Each

outrigger site will host a similar cylindrical dish. DRAO also has a hydrogen maser for high precision clocking, but not every outrigger site will have access to a hydrogen maser. Work has been done within CHIME to reduce the clocking errors for sites without a maser ([30]).

Compared to the Very Long Baseline Array (VLBA) with a maximum baseline of 8611 kilometers, the observing frequencies overlap completely on the lower end ([31]). However, the VLBA observes a much larger range of frequencies from 300MHz – 96 GHz compared to 400-800 MHz for CHIME Outriggers. With a focus at lower frequencies, the typical Very Long Baseline Interferometry (VLBI) calibrators are only studied at higher frequencies. Typically, VLBI calibrators have larger intrinsic morphologies and do not have observed fluxes at frequencies needed for CHIME Outriggers. For example, we also know the low frequency structure of radio galaxies, steeper spectrum, looks very different than high frequency structure, flatter spectrum. This is due to the lobes being brighter than the core at lower frequencies. These calibrators work well at high frequencies when their cores are much brighter. See 6.1 for an example of typical radio galaxy spectra.

Pulsars are an ideal substitute for most typical VLBI calibrators. Pulsars may show scattering towards lower frequencies, but we show that the effect is below a reasonable threshold in our chosen calibration set. They are also time domain separated, such that they can be easily distinguished from the background (although this is not relevant at such accurate localizations as those achieved with VLBI).

In VLBI, it is essential for correct localization of signals that the localization of a

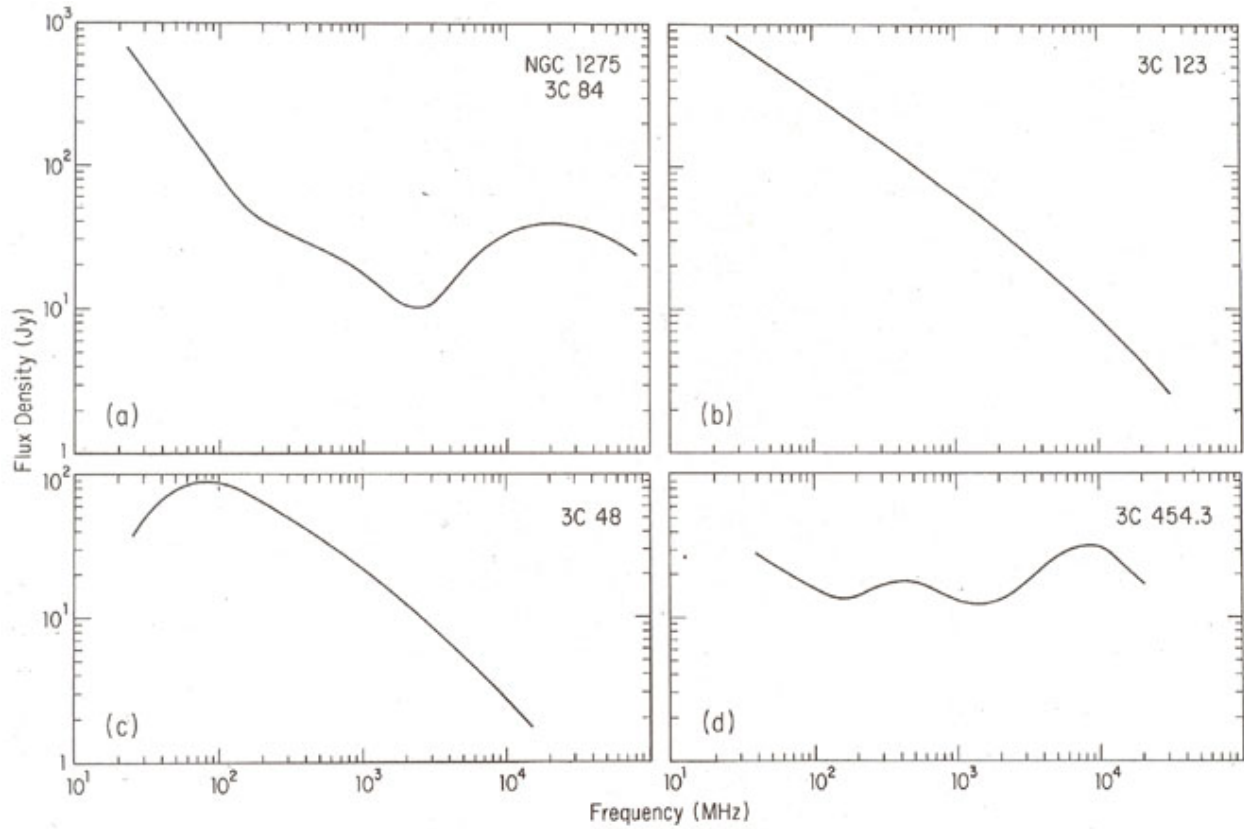


Figure 6.1: Example spectra of a few radio galaxies (top panel) and quasars (bottom panel) Credit https://ned.ipac.caltech.edu/level5/Sept04/Kellermann2/Kellermann1_3.html

calibrator is known extremely precisely. Pulsars can be localized on the milliarcsecond (mas) scale by VLBI and timing in their respective reference frames, International Celestial Reference Frame (ICRF) and barycentric. At lower frequencies, this becomes more important as the ionospheric effects increase as the frequency approaches the plasma frequency (approximately 20 MHz). Waves are refracted more the closer they are to the plasma frequency. With a proper pulsar calibrator in the field of view at all times, these effects can be somewhat mitigated.

6.1 Ideal Pulsar Calibrators

Our ideal pulsar calibrators have a signal to noise ratio (S/N) *as measured with CHIME* greater than 50 (25 in cross-correlation), localized to less than 10 mas (preferably less than or equal to 1 mas) in RA/DEC and scattering angle less than 10 mas. The minimum signal to noise ratio and maximum localization error allows for suitable calibration of outriggers. There is a 50 mas error budget for outriggers where approximately 40 mas are allocated to systematics. This leaves the remaining 10 mas to positional uncertainty in well localized pulsar calibrators. We want to ensure a S/N greater than the target S/N and suitable for calibration. We note that scattering angle is proportional to the scattering time. We expect more scattering for pulsars that lie along lines of sight with higher densities of free electrons. The calibrator localization error is also needed to measure our target's localization error since our calibration involves measuring the separation between the calibrator and source.

Minimum S/N (cross-corr. @ ARO/GBO)	Max Error on Localization RA/DEC	Max Scattering Angle
50 (25)	10 mas	10 mas

We find that we are able to satisfy this criteria with pulsars at many RA hours, but we also look to a follow up VLBI survey with the VLBA to fill in the gaps.

6.2 Combining CHIME and ATNF Pulsar data

As the CHIME Pulsar instrument is fully operational and commensal in its observation of pulsars, we already have a long list of pulsars observed with CHIME. CHIME Pulsar has even made new pulsar discoveries, such as J2108+45 and J0854+54. CHIME Pulsar detections can help inform CHIME Outriggers about suitable calibrators with S/N measurements at the relevant observing frequencies. These S/N measurements are made more useful by combining their best localizations from the Australia Telescope National Facility (ATNF) catalog. The full catalog can be found on the ATNF Website [32].

We create a list pulsars that are well localized, compact and bright enough to be suitable calibrators as a function of RA. We set criteria for the S/N, localization error in RA/DEC and scattering angle such that only pulsars which meet all these constraints (shown in the table in section 6.1) are included in our list. For simplicity and to normalize across pulsars with different lengths of observations, the S/N has been calculated assuming a 10 minute integration time as described in section 6.3 below. If pulsars are at a high enough declination,

we also add in both the lower and upper transits of the pulsars as potential calibrators.

6.3 Pulsar S/N

Normalized Pulsar S/N

The CHIME pulsar S/N is the ratio between the on pulse signal strength relative to the off pulse noise (7.1 in [33]):

This is determined with the following

$$S/N_{pulsar} = \frac{1}{\sigma_p \sqrt{W_{eq}}} \sum_{i=1}^{n_{bins}} (p_i - \mu_p) \quad (6.1)$$

where μ_p and σ_p are the mean and standard deviation of the off-pulse, respectively. W_{eq} is the equivalent width of the pulse, or the width of a top hat function with the same area and peak height as the pulse profile. p_i is the amplitude value of the i -th phase bin which is summed over the n_{bins} phase bins in the profile.

The CHIME/Pulsar instrument observes pulsars for various integration times per transit, depending on declination. Here we assume integration times of 10 minutes to facilitate comparison.

Cross-Correlation S/N

CHIME has 8 times the collecting area of the ARO and GBO outrigger sites, and 16 times the collecting area of the Allenby site. In autocorrelation, we can determine the S/N as follows:

$$S/N_{auto} \propto \sqrt{A_{core}^2} = A_{core}, \quad (6.2)$$

but in cross correlation:

$$S/N_{cross} \propto \sqrt{2A_{core}A_{outrigger}}, \quad (6.3)$$

The factor of 2 in equation 6.3 comes from the fact that the S/N scales as the square root of the number of baselines. We have $n^2/2$ (ignoring the internal baseline factor of $m^2/2$ since it's negligible) baselines that form the core in autocorrelation and nm baselines in cross-correlation between the core and the outrigger. If we take the ratio of these:

$$\frac{S/N_{cross}}{S/N_{auto}} \propto \sqrt{\text{baselines}} \quad (6.4)$$

$$\frac{S/N_{cross}}{S/N_{auto}} \propto \sqrt{\frac{nm}{n^2/2}} \quad (6.5)$$

$$\frac{S/N_{cross}}{S/N_{auto}} \propto \sqrt{\frac{2m}{n}} \quad (6.6)$$

Substituting, m for $A_{outrigger}$ and n for A_{core} :

$$\frac{S/N_{cross}}{S/N_{auto}} \propto \sqrt{\frac{2A_{outrigger}}{A_{core}}}, \quad (6.7)$$

and we know $S/N_{auto} = A_{core}$. As seen in equation 6.3, we have the following:

$$S/N_{cross} \propto \sqrt{2A_{outrigger}A_{core}}. \quad (6.8)$$

Due to the differences in collecting areas between CHIME (core) and ARO or GBO (outriggers), this becomes

$$S/N \sim \sqrt{2A_{core}A_{core}/8} = A_{core}/2 \quad (6.9)$$

or for Allenby

$$S/N \sim \sqrt{2A_{core}A_{core}/16} = \frac{\sqrt{2}}{4} A_{core}. \quad (6.10)$$

Scaled S/N to Latitude

We can also consider the scaled S/N at the GBO or ARO latitude (Allenby's latitude is very similar to CHIME's). This scaling is due to the difference in zenith angle and the sensitivity of the primary beam since CHIME is a zenith pointing instrument. The latitudes are tabulated below:

GBO Latitude	ARO Latitude	Allenby Latitude	CHIME Latitude
38.4330°	45.9556°	49.4167°	49.3208°

We can make a first order correction to the S/N detectable at GBO or ARO from the CHIME normalized S/N with a scale factor as follow:

$$S/N_{GBO||ARO} = S/N_{CHIME} \frac{\cos(DEC_{pulsar} - latitude_{GBO||ARO})}{\cos(DEC_{pulsar} - latitude_{CHIME})} \quad (6.11)$$

6.4 Localization Precision

Reference Frames: ICRF vs Barycentric

Before examining the localization errors of pulsars, we must recognize the caveat in these localizations. Pulsars can be localized through timing and VLBI experiments; however, both of these methods use a different reference frame. Pulsar timing uses the barycentric frame—in terms of the almost inertial Solar System center of mass, thus using a dynamical ephemeris. The pulse measured on an observatory on Earth must be corrected to the barycentric frame. VLBI relies on the ICRF as its reference frame which references extremely precise equatorial coordinates of extragalactic radio sources, such as quasars or active galaxies. It's a permanent reference frame and a replacement for J2000. With timing measurements, a pulsar's parallax is much harder to detect than using the ICRF coordinate system (see [34]).

These two coordinate systems must be noted, and the discrepancy in localizations between the two must be accounted for and eventually included in the errors of these pulsars. Though not included in this report, it is a calculation that must be made prior to blindly using the localizations of pulsars and their respective errors. These can be corrected somewhat well by comparing both timing and VLBI localizations of millisecond pulsars. Although the errors are not corrected here, the reference frame of the localization can be deduced by examining the survey of the pulsar.

ATNF Catalog Localizations

We then use the ATNF catalog to extract more information from all pulsars detected by CHIME beyond the CHIME S/N. The RA/DEC from the ATNF catalog are corrected for proper motion and used for the pulsar positions in this study. The list we employ does not contain all 1407 pulsars above about -20 degrees declination (the lowest declination value in the observed CHIME Pulsar list) in the ATNF catalog ¹. CHIME Pulsar has observed around 571 pulsars so far, and we assume that the other pulsars are among those not currently observed with CHIME Pulsar. See figure 6.2 below. The observation queue of CHIME Pulsar has been edited to prioritize these missing pulsars.

¹Note that Rotating Radio Transients (RRATs) are not included in this number.

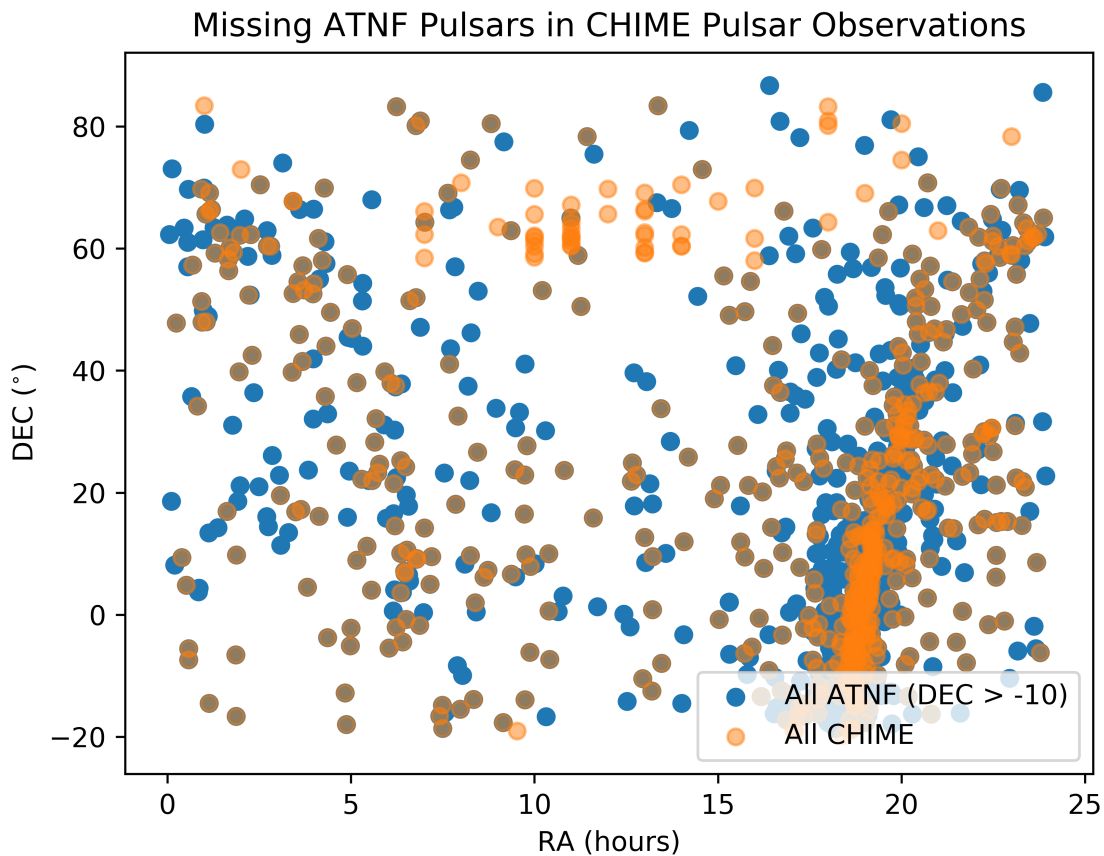


Figure 6.2: 837 pulsars from the ATNF catalog have not yet been observed by CHIME but are visible in the CHIME field of view.

We add the PM error in quadrature to arrive at the final RA (or DEC) error as follows ²

$$RA_{tot,err} = \sqrt{RA_{err}^2 + PM_{RA,err}^2} \quad (6.12)$$

²Note that other factors could affect this localization error, e.g., reference frame, and should be accounted for when making the final error calculation.

6.5 Scattering Angle

Measured ATNF Scattering Times

As an initial pass, we take the *measured* ATNF scattering times to calculate scattering angles of our potential pulsar calibrators and extrapolate them to CHIME frequencies. The scattering times are converted into scattering angles by first scaling the time to a CHIME observing frequency. We take 400MHz for this example. From the Kolmogorov power spectrum (the energy spectrum of turbulence in neutral gas), we know scattering times scale as $\nu^{-4.4}$ ([35]).

$$\tau_{400MHz} = \tau_{1GHz} \frac{400MHz^{-4.4}}{1GHz^{-4.4}} \quad (6.13)$$

To convert scattering time into scattering angle, we proceed with equation A15 in [36]:

$$\theta_{400MHz} = \sqrt{\frac{16 \ln(2) c \tau_{400MHz}}{d_{pulsar}}} \quad (6.14)$$

Unfortunately, there are many pulsars with missing measured scattering times in the ATNF catalog. To find an alternative way to calculate this, we turn to the the NE2001 Galactic Free Electron Density Model from [37]. We maintain uniformity by using the scattering time calculated from the NE2001 model for *all* pulsars rather than using it to fill in the missing scattering times for certain pulsars.

NE2001 Model

The intergalactic medium has clumpiness that's very difficult to model and contributes to inaccuracy in the NE2001 model. There are other models that calculate this, and a notable one is the YMW16 model ([38]). They're commonly used to predict distances of pulsars given DM measurements. However, these models' accuracies is disputed and has been shown to cause large discrepancies. For example in [39], they determine the distance to PSR J08372454 as 0.2 and 0.9 kpc using $H\alpha$ and a supernova remnant, respectively. The YMW16 model predicts a distance greater than 25 kpc, and the NE2001 model predicts a distance of 6.3kpc.

We choose the NE2001 model because of its common use in the literature. The NE2001 model describes the galactic distribution of free electrons. By specifying galactic coordinates of a pulsar, we can obtain estimates for the scattering times of the pulsars. The scattering times are then converted to angles using equations 6.13 through 6.14. The Python module `pyne2001` is used to calculate these scattering times with the ATNF values for galactic longitude, latitude and distance.

6.6 Results

The object-oriented analysis code can be found on GitHub at <https://github.com/sabrinastronomy/PulsarCalibrators>. The ATNF catalog or

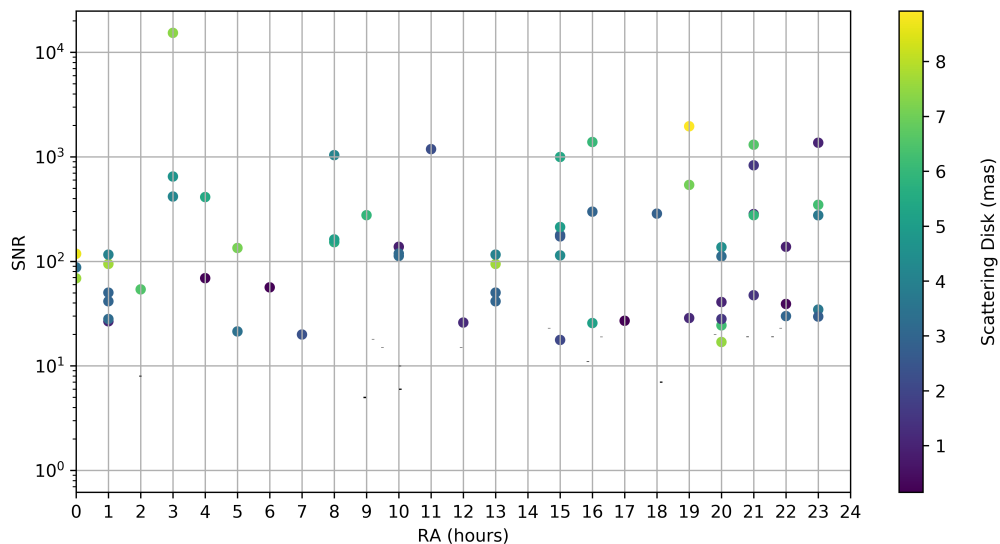


Figure 6.3: Pulsars detectable by CHIME falling with our S/N and localization error constraints (less than 10 mas). The color denotes the scattering angle of the pulsar.

combined ATNF/CHIME datasets can be easily queried in their respective classes.

Overall, there are 65 ideal pulsar calibrators that fall within the localization, S/N, and scattering angle constraints (where the upper and lower transits of a pulsar count as a total of two pulsars). When including transits, we are only missing pulsars at one RA hour (RA = 14) for our ideal pulsar calibrators (see figure 6.3). The current median distance in time to the nearest pulsar crossing is 9 minutes.

However, many of our analyzed pulsars lacked localization precision that will be possible with further VLBI follow-up. A VLBA proposal was submitted in August, 2020 to fill in and increase the number of pulsars at certain RA hours. It was accepted and granted 60 hours of time to observe. Observations are currently underway.

Chapter 7

GNSS Satellites: A novel VLBI calibration method

There have been many proposed methods for mitigating ionospheric effects. Though some are useful to radio telecommunications, e.g., Skywave propagation, most greatly disrupt precision in the science done at lower and lower radio frequencies. The ionosphere total electron content (TEC) has been explored in many studies characterizing the ionospheric properties, e.g., [40] and [41]. When the TEC is known, correcting for ionospheric error becomes much easier. The variability of the ionosphere around the Earth is so great that many innovative methods for real time tracking of the ionosphere are still being explored. As seen in figure 5.4, the ionosphere plasma frequency is being tracked by ionosondes fairly frequently. In radio interferometry, there is still a need for realtime overhead analysis for different elements.

One of the most promising techniques for quantifying the total electron content in real time uses Global Positioning Satellites (GNSS) to track the total electron content in the ionosphere. Placing GNSS antennas at various elements of a radio interferometer observing lower frequencies could prove extremely useful in correcting for ionospheric effects.

GNSS satellites have been used before for ionospheric correction in VLBI (e.g., [42] and [43]). Their use in conjunction with CHIME pulsar calibrators to supplement ionospheric maps from global TEC measurements, e.g. Caltech/JPL's IARS: <https://iono.jpl.nasa.gov/index.html> will be extremely important in providing precise FRB localization measurements. We do not expect to have enough calibrators to continuously have one in CHIME's field of view. GNSS satellites could provide an excellent alternative to pulsar calibrators as there are always GNSS satellites visible by each CHIME Outrigger. If we have multiple GNSS satellites above at once, we may also be able to obtain multiple TEC measurements at various lines of sight corresponding to each satellite. Correcting for ionospheric delays is especially important because the CHIME frequency range (400-800MHz) is relatively low. This causes more refraction within the ionosphere and a larger delay relative to higher frequencies as described in 5. Precise ionospheric corrections through TECu measurements optimized with GNSS satellites may make the difference on whether we can localize an FRB to within its host galaxy or not. Motivated by the outriggers' strict timing error budget, the ionosphere correction needs to be accurate to approximately 300 picoseconds in order to reach our localization goal of less than 100

milliarcseconds, since

$$\Delta\theta \approx \frac{c}{b}\Delta\tau. \quad (7.1)$$

As an example, we take a baseline length of 3000km and an observing frequency of 600MHz. We can relate positional uncertainty and TEC values with the following expression (using equations 7.1 and 5.47):

$$\Delta\theta = 1.3 \times 10^{-3} \left(\frac{c}{b}\right) \left(\frac{DM}{TECu}\right) \left(\frac{1MHz}{\nu}\right)^2. \quad (7.2)$$

Thus, we can arrive at localizations of 100 mas or less if we know the TEC to 1.3 TECu. Examining the ionospheric metrics derived in [44], approximately 400 ionospheric pierce points (see figure 7.1) or about 20 calibrators spread evenly across the MWA field of view (625 deg^2) are required to maintain an understanding of the ionosphere at 200MHz. Since our frequencies of interest are 200MHz or more higher than this, we anticipate even less calibrators will be needed. GNSS satellites will greatly increase the number of potential calibrators that can be used in a similar analysis for CHIME Outriggers.

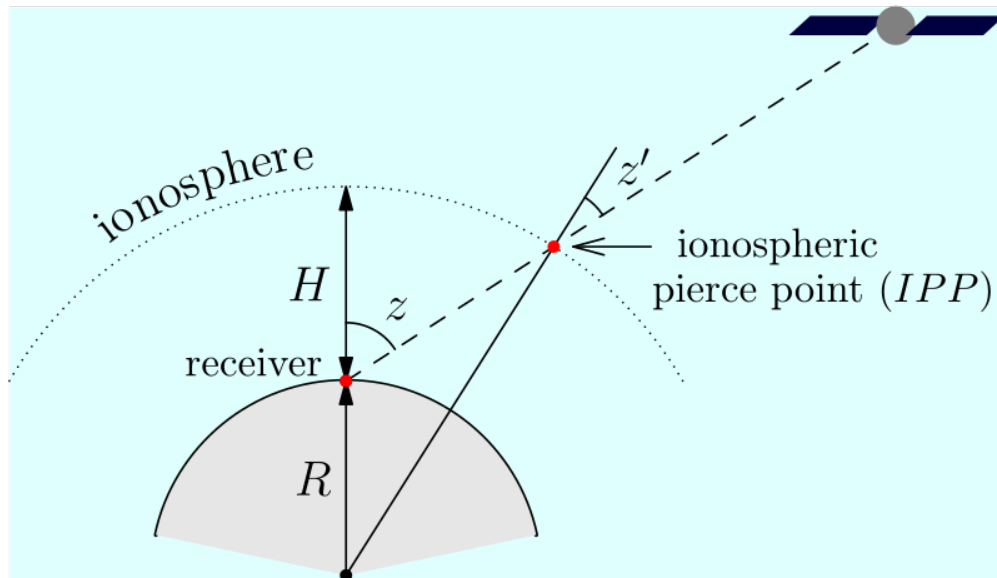


Figure 7.1: A depiction of an ionospheric pierce point. A signal from a satellite will cross the ionosphere at a pierce point before arriving at the receiver. Image Credi: Yury Kirienko

7.1 GNSS Antenna Prototype

CHIME ICE Board

In developing our prototype, we use existing hardware developed by the McGill Cosmology Group: the ICE board [45]. The ICE board can be used as an Analog to Digital Converter (ADC) for baseband data collection. We do not need to remove any circuitry from the existing ICE board which includes specific circuitry for CHIME data correlation and collection, i.e., the CHIME mezzanine. The GNSS frequencies L2 and L5 will alias into very similar signals, however. If we shift the FPGA sampling frequency down a few percent

to 385 or 400 MHz for example, we can avoid this somewhat. L1 has been the easiest frequency (1575 MHz) to observe with this setup to avoid aliasing.

GNSS Satellites

In the United States, there are currently approximately 31 GPS satellites in orbit to localize positions. This does not include the GLONASS (Russia) and GALILEO (European Union) satellites also used for global position. See 7.2 for an overview of all the potential satellites in the GNSS network that may be useful for this work. Each center frequency (Link1 = L1, Link5 = L5, etc.) is a multiple of the 10.23 MHz master GNSS clock, i.e., $L5 = 1176.45\text{MHz} = 115 \times 10.23\text{MHz}$. Note that this does not include satellite systems coming online in 2021, such as China's Beidou.

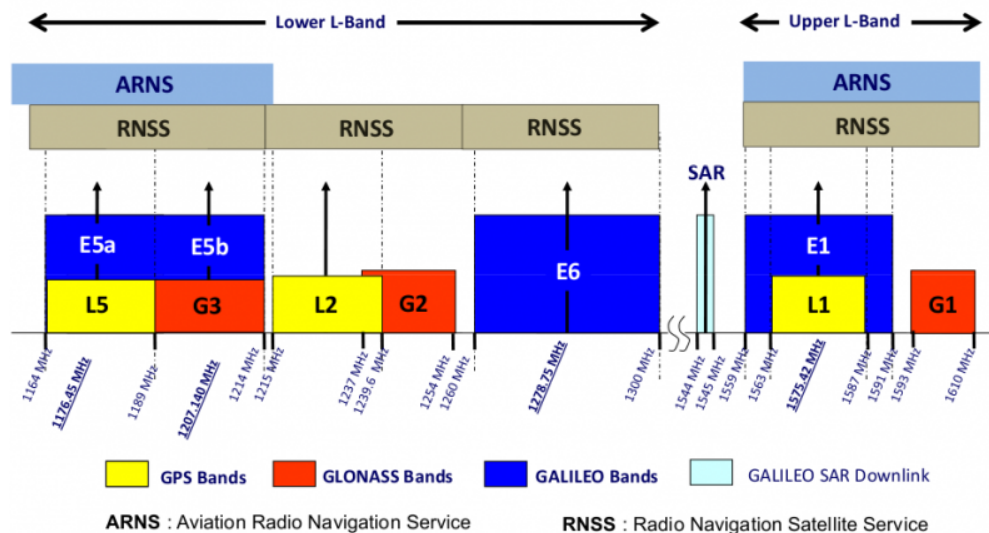


Figure 7.2: Frequency bands available for satellite observations.

We note that these frequencies do not fall within the CHIME Outriggers bandwidth. Although we may be able to see them through aliasing, we anticipate future instruments covering more of the GNSS band. The Canadian Hydrogen Observatory and Radio-transient Detector (CHORD) will build on CHIME's original infrastructure and will have an ultra wide band spanning from 300-1500MHz. GNSS frequencies fall almost entirely within the CHORD band and will be observable from the instrument itself. We also anticipate making use of an omnidirectional antenna external to the instrument to increase the number of satellites we can use to determine TEC. We can also direct the output from this antenna into ICE boards (described in [45]) as long as the analog low pass filters have been removed. ICE boards are the tools used for data acquisition in CHIME.

Observations of GNSS satellite signals are the primary method of localization around the world. With dual band frequency receivers, they allow centimeter level localization precision in open sky areas. GNSS error increases drastically when localizations are instead made in urban canyons in cities due to satellites being blocked, but this is not a problem in radio astronomy. On a fundamental level, the GNSS satellite modulates a carrier wave with a binary pseudorandom noise (PRN) code. Each satellite has its own corresponding PRN code which the receiver demodulates (See [46] and [47]). The modulation is done through the binary phase shift key (BPSK) modulation scheme. The binary message encoded in the PRN code is encoded into two different phases of the carrier wave. $\theta = 0^\circ$ corresponds to a binary value of 1 and $\theta = 180^\circ$ corresponds to a binary value of 0. See figure 7.3 for a

visualization.

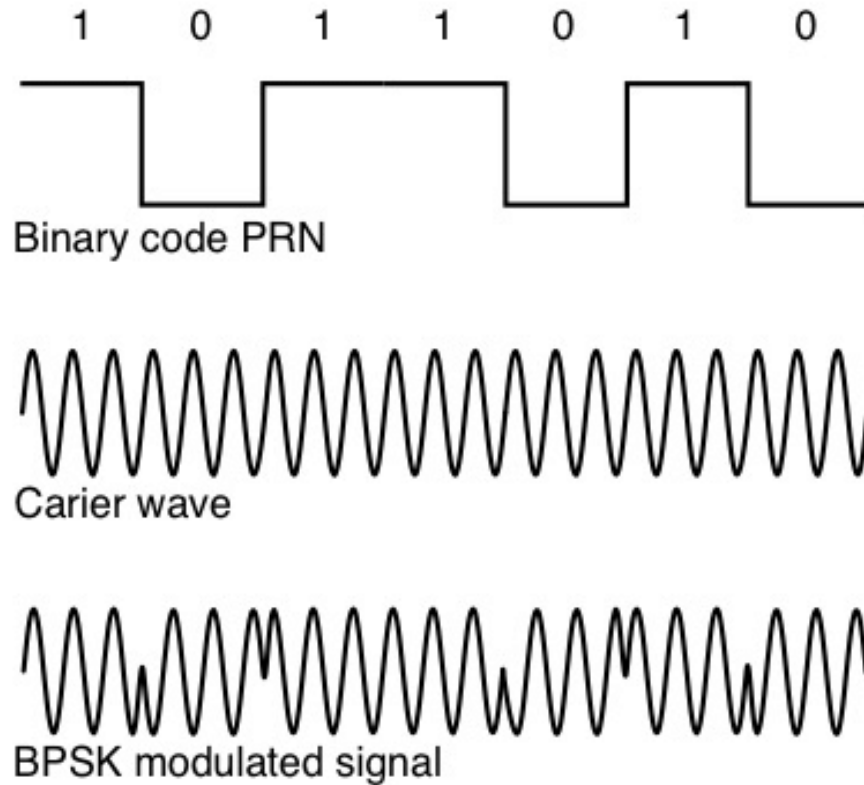


Figure 7.3: A graphic depicting various individual stages of the GNSS satellite modulation scheme.

7.2 Methods

Although we have not yet successfully applied GNSS satellites to calibration for the ionosphere, we have created a full plan to implement this method. We expect to receive approximately 10 seconds of baseband data from a GNSS antenna in the McGill

Cosmology Lab. We can then apply the following post-processing:

1. **Baseband to usable data** - We first convert binary baseband data from the ADC into a voltage time stream that we can fast fourier transform (FFT).
2. **GNSS signal extraction** - FFT data using SDR (software defined radio) or other, window and extract desired GNSS carrier signal frequencies. This is where our current research has brought us. We utilize GNSS SDR from [48]. In figure 7.4, we see the amplitude peaks for various delays and doppler effects. These are not yet ionospheric delays but show code phases that are checked by the SDR to lock onto the signal. This is data from the Baryon Mapping Experiment (BMX) radio telescope at Stony Brook University. The BMX data is showing us that our acquisition is not great with our initial attempt to funnel data into an SDR. In figure 7.5, we can see what an excellent acquisition of the GNSS signal looks like.

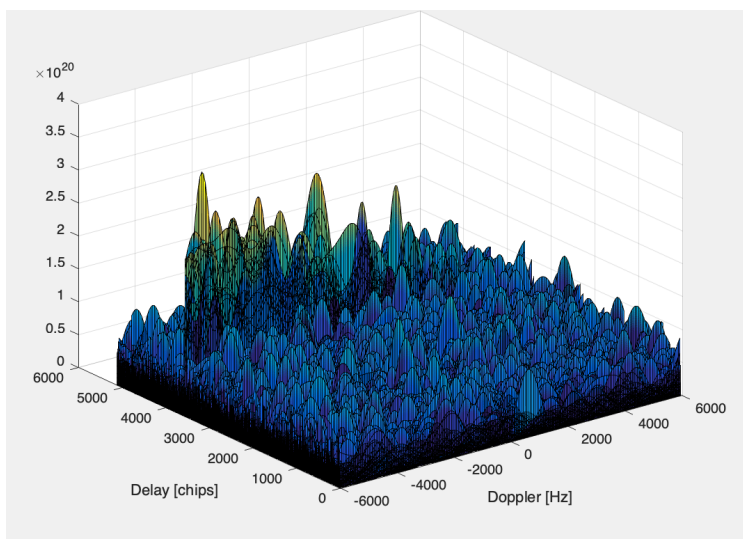


Figure 7.4: Output from GNSS SDR with BMX data and a poor acquisition.

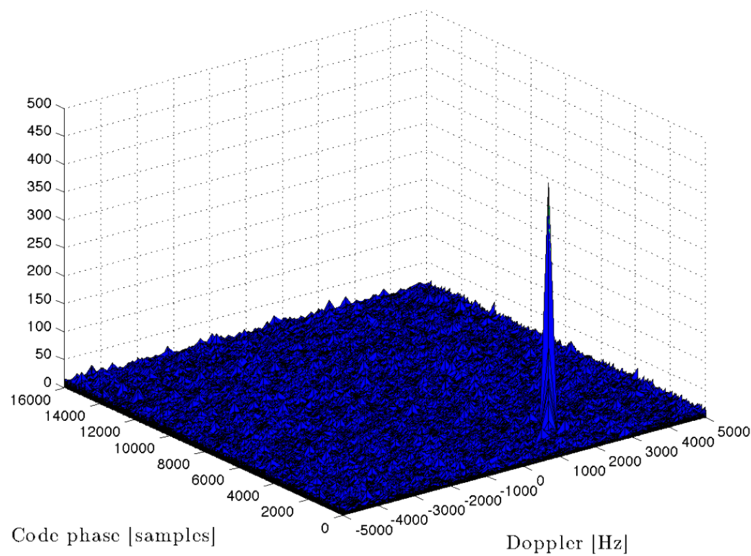


Figure 7.5: Ideal output from GNSS SDR with an excellent acquisition. Credit: GNSS SDR

3. Get a time delay between two GNSS frequencies - We will compare the delays

due to the ionosphere between L1 and other lower GNSS frequencies from the same satellite. The difference in these two delays tells us the time delay due to the ionosphere. Note that we don't need access to a master clock here to compare the times to. We use the relative delay. With a proper acquisition as seen in figure 7.5, we can extract multiple pseudoranges. Pseudoranges are the distances that your receiver thinks the satellite is and account for ionospheric effects. We expect larger pseudoranges (larger time delay) at lower frequencies. From the pseudorange, we can easily derive a time delay.

4. **TECu measurement** - We can convert the time delay to the TECu to determine the ionospheric strength in the line of site of the satellite. When using a physical GNSS receiver, we have been able to obtain excellent acquisitions and derive preliminary sTEC measurements as seen in figure 7.6, where sTEC refers to slanted TEC measurements as a function of elevation.

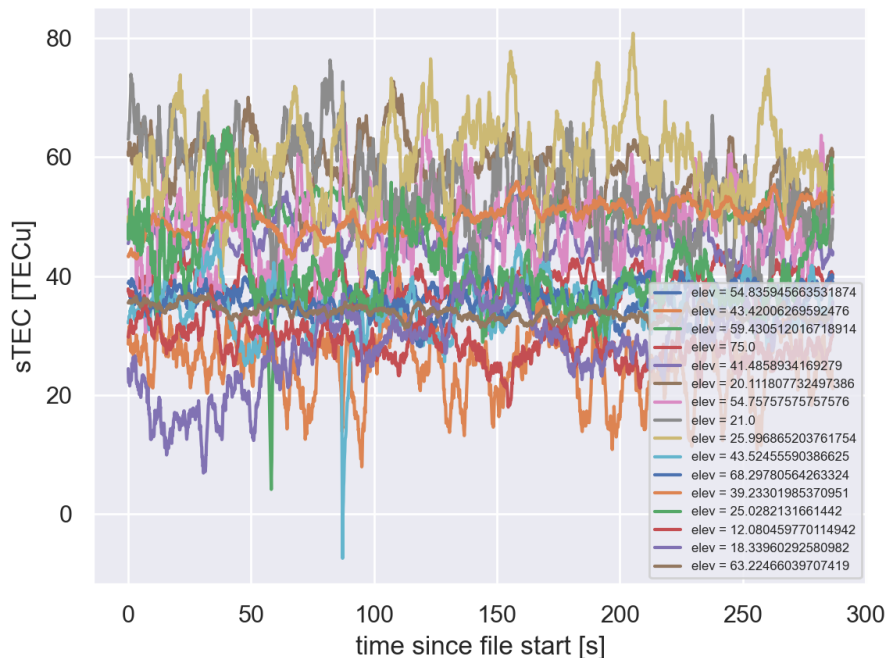


Figure 7.6: Preliminary plot of sTECs versus time using a GNSS receiver.

Because of the high number of GNSS satellites available at one time, we anticipate this being a powerful tool to calibrate ionosphere effects. In the field with the GNSS receiver, we've seen a maximum of about 40 satellites at a time with an unobstructed sky view. Taking a optimistic CHIME field of view including side lobes of $400deg^2$ as an example, we can estimate the number of satellites in the field of view at a time as approximately 1 (using the ratio of $400deg^2$ over half of a hemisphere $2\pi sr = 20626deg^2$ to approximate the number of satellites). We note that these satellites could still be many degrees away from the FRB. However, this does not include the side lobes, and we actually expect this to be

an underestimate especially with a larger beam antenna.

If we have detections of the L1 and L5 signals from a single satellite in the GNSS constellation, we can take a brief look at how we would calculate the ionospheric delay. We know that the ionospheric time delay, τ , is proportional to one over frequency squared;

$$\tau \propto \beta \nu^{-2}, \quad (7.3)$$

where β includes the angular zenith offset and total vertical electron content factor. If we take the ionospheric time delays at L1 and L5 frequencies, we cancel out the pseudorange delay as well. We can calculate the ionospheric delay using the arrival times of L5 and L1, τ_{L5} and τ_{L1} , respectively as follows:

$$\Delta\tau = \tau_{L5} - \tau_{L1} = \frac{\beta}{\nu_{L5}^2} - \frac{\beta}{\nu_{L1}^2} \approx 0.79 \frac{\beta}{\nu_{L1}^2} \approx 0.79 \tau_{ionosphere}. \quad (7.4)$$

If we consider the bandwidth of the GNSS signal, approximately 10MHz, we can estimate an ionospheric timing precision of about 100 nanoseconds using bandwidth over S/N. We took a S/N of 1, but if we can integrate the signal for even a few seconds longer, we expect this to go up to 1000. This puts us at 100 picoseconds of timing precision which is within the error budget of 300 picoseconds for CHIME Outriggers.

We also note that because of the incredible daily data creation size already expected by CHIME Outriggers, adding a few timestreams with GNSS data into the correlator does not

make a drastic difference. We understand exactly what GNSS signals should look like and can cross-correlate this against the incoming datastreams. This will enable detection and monitoring of GNSS signals with high S/N clocked at the same time as the astrophysical observations. As an example for the upcoming Canadian Hydrogen Observatory and Radio Transient Detector (CHORD), adding twenty signals will increase the load on the correlator by 10%. Whereas with the VLBA, this effect is 300%.

Both GNSS satellites and pulsars were presented as calibrators in this work. We hope both the artificial and astrophysical calibrators can complement each other. GNSS satellites have several advantages over pulsars. The changing elevation of GNSS satellites (approximately 0.1 degree per minute) eases the creation of beam maps for an instrument. We will also have continuous opportunity to determine TEC because of the slow rate at which GNSS satellites move. This ensures that we will *always* have some measurement of TEC at the time an FRB is viewed. This is not possible with pulsar calibrators. Although there will always be some uncertainty in TEC, this uncertainty grows with distance from the calibrator. We anticipate that there will always be more GNSS satellites than pulsars above the horizon and visible by an omnidirectional antenna placed near VLBI instrument. This gives a higher probability that the satellite will be closer to the FRB (or other transient) and will allow ionospheric calibration to be more precise in the future. Overall, we expect better localizations of astrophysical phenomena through this calibration method.

The remainder of this work will be done during the PhD of this thesis' author.

Chapter 8

Conclusion

We began this thesis with a brief overview of cosmology, with an emphasis on the CMB and reionization, and the use of the 21-cm line. We then built intuition for Bayesian statistics. We derived the analytic posterior for a toy model, and then moved onto a realistic likelihood to use in our MCMC and HMC to sample the posterior of the density field from a temperature brightness field. We sample the posterior containing this likelihood to find the probability of a matter density field given an observed brightness temperature field and a redshift. We showed proof of concept with a 1D universe and explored how the error will increase as we go to lower redshifts. Within the constraints of a 1D universe and at low ionization fractions, there seems to be enough information in the brightness temperature field to infer the density field during reionization to some degree. We expect to need many hundreds to thousands of hours on a supercomputer to thoroughly sample the posterior distribution of the matter

density field as we increase the number of pixels and go to 3D. This is the case despite using an analytic gradient of our likelihood with an HMC. We leave this for future work.

In the latter part of the thesis, we describe why it is that the ionosphere hinders low frequency radio astronomy. We then go on to discuss pulsars as calibrators being a potential solution to this issue to mitigate time delays. We found that pulsars will help calibrate CHIME Outriggers but follow up localization and observation of many pulsars with the VLBA is needed for them to serve as proper calibrators. Lastly, we discussed an initial exploration of using GNSS satellites to determine line of site TEC_u measurements within the ionosphere. This method has shown some initial promise and will be the topic of the writer's PhD thesis. Eventually, we hope this technique will be useful in sub-milliarcsecond localizations of fast radio bursts and other relevant astronomical applications, such as beam calibrations.

Although the topics in this thesis are varied, well localized fast radio bursts with redshifts will likely eventually be a useful cosmological probe. Making use of characteristics of FRBs could be useful in constraining parameters describing reionization. Although this topic is not explored in this thesis, we hope this provides a useful link between these two very diverse projects.

Bibliography

- [1] Planck Collaboration, N. Aghanim, Y. Akrami, M. Ashdown, J. Aumont, C. Baccigalupi, M. Ballardini, A. J. Banday, R. B. Barreiro, N. Bartolo, S. Basak, R. Battye, K. Benabed, J. P. Bernard, M. Bersanelli, P. Bielewicz, J. J. Bock, J. R. Bond, J. Borrill, F. R. Bouchet, F. Boulanger, M. Bucher, C. Burigana, R. C. Butler, E. Calabrese, J. F. Cardoso, J. Carron, A. Challinor, H. C. Chiang, J. Chluba, L. P. L. Colombo, C. Combet, D. Contreras, B. P. Crill, F. Cuttaia, P. de Bernardis, G. de Zotti, J. Delabrouille, J. M. Delouis, E. Di Valentino, J. M. Diego, O. Doré, M. Douspis, A. Ducout, X. Dupac, S. Dusini, G. Efstathiou, F. Elsner, T. A. Enßlin, H. K. Eriksen, Y. Fantaye, M. Farhang, J. Fergusson, R. Fernandez-Cobos, F. Finelli, F. Forastieri, M. Frailis, A. A. Fraisse, E. Franceschi, A. Frolov, S. Galeotta, S. Galli, K. Ganga, R. T. Génova-Santos, M. Gerbino, T. Ghosh, J. González-Nuevo, K. M. Górski, S. Gratton, A. Gruppuso, J. E. Gudmundsson, J. Hamann, W. Handley, F. K. Hansen, D. Herranz, S. R. Hildebrandt, E. Hivon, Z. Huang, A. H. Jaffe, W. C. Jones, A. Karakci, E. Keihänen, R. Keskitalo, K. Kiiveri, J. Kim, T. S. Kisner, L. Knox, N. Krachmalnicoff,

- M. Kunz, H. Kurki-Suonio, G. Lagache, J. M. Lamarre, A. Lasenby, M. Lattanzi, C. R. Lawrence, M. Le Jeune, P. Lemos, J. Lesgourgues, F. Levrier, A. Lewis, M. Liguori, P. B. Lilje, M. Lilley, V. Lindholm, M. López-Caniego, P. M. Lubin, Y. Z. Ma, J. F. Macías-Pérez, G. Maggio, D. Maino, N. Mandolesi, A. Mangilli, A. Marcos-Caballero, M. Maris, P. G. Martin, M. Martinelli, E. Martínez-González, S. Matarrese, N. Mauri, J. D. McEwen, P. R. Meinhold, A. Melchiorri, A. Mennella, M. Migliaccio, M. Millea, S. Mitra, M. A. Miville-Deschênes, D. Molinari, L. Montier, G. Morgante, A. Moss, P. Natoli, H. U. Nørgaard-Nielsen, L. Pagano, D. Paoletti, B. Partridge, G. Patanchon, H. V. Peiris, F. Perrotta, V. Pettorino, F. Piacentini, L. Polastri, G. Polenta, J. L. Puget, J. P. Rachen, M. Reinecke, M. Remazeilles, A. Renzi, G. Rocha, C. Rosset, G. Roudier, J. A. Rubiño-Martín, B. Ruiz-Granados, L. Salvati, M. Sandri, M. Savelainen, D. Scott, E. P. S. Shellard, C. Sirignano, G. Sirri, L. D. Spencer, R. Sunyaev, A. S. Suur-Uski, J. A. Tauber, D. Tavagnacco, M. Tenti, L. Toffolatti, M. Tomasi, T. Trombetti, L. Valenziano, J. Valiviita, B. Van Tent, L. Vibert, P. Vielva, F. Villa, N. Vittorio, B. D. Wandelt, I. K. Wehus, M. White, S. D. M. White, A. Zacchei, and A. Zonca, “Planck 2018 results. VI. Cosmological parameters,” , vol. 641, p. A6, Sept. 2020.
- [2] D. Tseliakhovich, R. Barkana, and C. M. Hirata, “Suppression and spatial variation of early galaxies and minihaloes,” *Monthly Notices of the Royal Astronomical Society*, vol. 418, p. 906–915, Sep 2011.
- [3] K. Ota, M. Iye, N. Kashikawa, A. Konno, F. Nakata, T. Totani, M. A. R. Kobayashi,

- Y. Fudamoto, A. Seko, J. Toshikawa, and et al., “A new constraint on reionization from the evolution of the lyluminosity function atz 6–7 probed by a deep census ofz= 7.0 lyemitter candidates to 0.31*,” *The Astrophysical Journal*, vol. 844, p. 85, Jul 2017.
- [4] M. Betancourt, “A conceptual introduction to hamiltonian monte carlo,” 2018.
- [5] N. Battaglia, H. Trac, R. Cen, and A. Loeb, “Reionization on Large Scales. I. A Parametric Model Constructed from Radiation-hydrodynamic Simulations,” , vol. 776, p. 81, Oct. 2013.
- [6] M. Pagano and H. Fronenberg, “Constraining the Epoch of Reionization With Highly Dispersed Fast Radio Bursts,” *arXiv e-prints*, p. arXiv:2103.03252, Mar. 2021.
- [7] R. H. BRANDENBERGER, “Alternatives to the inflationary paradigm of structure formation,” *International Journal of Modern Physics: Conference Series*, vol. 01, p. 67–79, Jan 2011.
- [8] A. Heger and S. E. Woosley, “The Nucleosynthetic Signature of Population III,” , vol. 567, pp. 532–543, Mar. 2002.
- [9] S. R. Furlanetto, S. P. Oh, and F. H. Briggs, “Cosmology at low frequencies: The 21 cm transition and the high-redshift Universe,” , vol. 433, pp. 181–301, Oct. 2006.
- [10] S. R. Furlanetto, “The 21-cm line as a probe of reionization,” *Astrophysics and Space Science Library*, p. 247–280, 2016.

-
- [11] T. J. W. Lazio, N. E. Kassim, W. C. Erickson, B. C. Hicks, P. C. Crane, K. P. Stewart, P. S. Ray, K. W. Weiler, and L. J. Rickard, “The Low Frequency Array (LOFAR): Opening a New Window on the Universe,” in *American Astronomical Society Meeting Abstracts #200*, vol. 200 of *American Astronomical Society Meeting Abstracts*, p. 64.01, May 2002.
- [12] N. Fagnoni and E. de Lera Acedo, “The Hydrogen Epoch of Reionization Array (HERA). Improvement of the antenna response with a matching network and scientific impacts,” *arXiv e-prints*, p. arXiv:1606.08701, June 2016.
- [13] D. Mitchell, L. Greenhill, R. Wayth, S. Ord, R. Sault, S. Doeleman, J. Kasper, and M. Morales, “The Murchison Widefield Array Real-Time System,” in *American Astronomical Society Meeting Abstracts*, vol. 211 of *American Astronomical Society Meeting Abstracts*, p. 11.03, Dec. 2007.
- [14] D. Foreman-Mackey, D. W. Hogg, D. Lang, and J. Goodman, “emcee: The mcmc hammer,” *Publications of the Astronomical Society of the Pacific*, vol. 125, p. 306–312, Mar 2013.
- [15] J. Goodman and J. Weare, “Ensemble samplers with affine invariance,” *Communications in Applied Mathematics and Computational Science*, vol. 5, pp. 65–80, Jan. 2010.
- [16] J. Salvatier, T. V. Wiecki, and C. Fonnesbeck, “Probabilistic programming in python using pymc3,” *PeerJ Computer Science*, vol. 2, p. e55, 2016.

- [17] T. T. D. Team, R. Al-Rfou, G. Alain, A. Almahairi, C. Angermueller, D. Bahdanau, N. Ballas, F. Bastien, J. Bayer, A. Belikov, A. Belopolsky, Y. Bengio, A. Bergeron, J. Bergstra, V. Bisson, J. B. Snyder, N. Bouchard, N. Boulanger-Lewandowski, X. Bouthillier, A. de Brébisson, O. Breuleux, P.-L. Carrier, K. Cho, J. Chorowski, P. Christiano, T. Cooijmans, M.-A. Côté, M. Côté, A. Courville, Y. N. Dauphin, O. Delalleau, J. Demouth, G. Desjardins, S. Dieleman, L. Dinh, M. Ducoffe, V. Dumoulin, S. E. Kahou, D. Erhan, Z. Fan, O. Firat, M. Germain, X. Glorot, I. Goodfellow, M. Graham, C. Gulcehre, P. Hamel, I. Harlouchet, J.-P. Heng, B. Hidasi, S. Honari, A. Jain, S. Jean, K. Jia, M. Korobov, V. Kulkarni, A. Lamb, P. Lamblin, E. Larsen, C. Laurent, S. Lee, S. Lefrancois, S. Lemieux, N. Léonard, Z. Lin, J. A. Livezey, C. Lorenz, J. Lowin, Q. Ma, P.-A. Manzagol, O. Mastropietro, R. T. McGibbon, R. Memisevic, B. van Merriënboer, V. Michalski, M. Mirza, A. Orlandi, C. Pal, R. Pascanu, M. Pezeshki, C. Raffel, D. Renshaw, M. Rocklin, A. Romero, M. Roth, P. Sadowski, J. Salvatier, F. Savard, J. Schlüter, J. Schulman, G. Schwartz, I. V. Serban, D. Serdyuk, S. Shabanian, Étienne Simon, S. Spieckermann, S. R. Subramanyam, J. Sygnowski, J. Tanguay, G. van Tulder, J. Turian, S. Urban, P. Vincent, F. Visin, H. de Vries, D. Warde-Farley, D. J. Webb, M. Willson, K. Xu, L. Xue, L. Yao, S. Zhang, and Y. Zhang, “Theano: A python framework for fast computation of mathematical expressions,” 2016.
- [18] M. D. Hoffman and A. Gelman, “The no-u-turn sampler: Adaptively setting path

- lengths in hamiltonian monte carlo,” 2011.
- [19] F. List and G. F. Lewis, “A unified framework for 21 cm tomography sample generation and parameter inference with progressively growing GANs,” , vol. 493, pp. 5913–5927, Apr. 2020.
- [20] A. Mesinger, “Reionization and cosmic dawn: theory and simulations,” *Proceedings of the International Astronomical Union*, vol. 12, no. S333, p. 3–11, 2017.
- [21] C. Modi, F. Lanusse, U. Seljak, D. N. Spergel, and L. Perreault-Levasseur, “Cosmicrim : Reconstructing early universe by combining differentiable simulations with recurrent inference machines,” 2021.
- [22] A. S. Academy, “History of ionospheric discovery.” <https://www.spaceacademy.net.au/library/notes/earlyion.htm>, March 2020. (Accessed on 03/09/2020).
- [23] S. S. Center, “Tracking solar flares.” <http://solar-center.stanford.edu/SID/activities/ionosphere.html>, March 2020. (Accessed on 03/09/2020).
- [24] U. B. A. Department and A. Polin, “Plasma frequency - astrobaki.” https://casper.ssl.berkeley.edu/astrobaki/index.php/Plasma_Frequency, March 2020. (Accessed on 03/09/2020).
- [25] E. Notes, “Ionospheric layers: D, e, f, f1, f2, regions electronics notes.” <https://www.electronics-notes.com/articles/antennas-propagation/>

- ionospheric/ionospheric-layers-regions-d-e-f1-f2.php, March 2020. (Accessed on 03/09/2020).
- [26] C. J. Lonsdale, R. J. Cappallo, M. F. Morales, F. H. Briggs, L. Benkevitch, J. D. Bowman, J. D. Bunton, S. Burns, B. E. Corey, L. Desouza, S. S. Doeleman, M. Derome, A. Deshpande, M. R. Gopala, L. J. Greenhill, D. E. Herne, J. N. Hewitt, P. A. Kamini, J. C. Kasper, B. B. Kincaid, J. Kocz, E. Kowald, E. Kratzenberg, D. Kumar, M. J. Lynch, S. Madhavi, M. Matejek, D. A. Mitchell, E. Morgan, D. Oberoi, S. Ord, J. Pathikulangara, T. Prabu, A. Rogers, A. Roshi, J. E. Salah, R. J. Sault, N. U. Shankar, K. S. Srivani, J. Stevens, S. Tingay, A. Vaccarella, M. Waterson, R. B. Wayth, R. L. Webster, A. R. Whitney, A. Williams, and C. Williams, “The Murchison Widefield Array: Design Overview,” *IEEE Proceedings*, vol. 97, pp. 1497–1506, Aug. 2009.
- [27] CHIME/FRB Collaboration, M. Amiri, K. Bandura, P. Berger, M. Bhardwaj, M. M. Boyce, P. J. Boyle, C. Brar, M. Burhanpurkar, P. Chawla, J. Chowdhury, J. F. Cliche, M. D. Cranmer, D. Cubranic, M. Deng, N. Denman, M. Dobbs, M. Fandino, E. Fonseca, B. M. Gaensler, U. Giri, A. J. Gilbert, D. C. Good, S. Guliani, M. Halpern, G. Hinshaw, C. Höfer, A. Josephy, V. M. Kaspi, T. L. Landecker, D. Lang, H. Liao, K. W. Masui, J. Mena-Parra, A. Naidu, L. B. Newburgh, C. Ng, C. Patel, U. L. Pen, T. Pinsonneault-Marotte, Z. Pleunis, M. Rafiei Ravandi, S. M. Ransom, A. Renard, P. Scholz, K. Sigurdson, S. R. Siegel, K. M. Smith, I. H. Stairs, S. P. Tendulkar, K. Vand

- erlinde, and D. V. Wiebe, “The CHIME Fast Radio Burst Project: System Overview,”
, vol. 863, p. 48, Aug. 2018.
- [28] E. Notes, “Skywaves: Skip distance, skip zone electronics notes.” <https://www.electronics-notes.com/articles/antennas-propagation/ionospheric/skywaves-skip-distance-zone.php>, March 2020. (Accessed on 03/09/2020).
- [29] A. S. Academy, “Radio astronomy and the ionosphere.” <https://www.spaceacademy.net.au/env/spwx/raiono.htm>, March 2020. (Accessed on 03/09/2020).
- [30] S. Cary, J. Mena-Parra, C. Leung, K. Masui, J. F. Kaczmarek, and T. Cassanelli, “Evaluating and enhancing candidate clocking systems for CHIME/FRB VLBI outriggers,” *Research Notes of the AAS*, vol. 5, p. 216, sep 2021.
- [31] P. J. Napier, D. S. Bagri, B. G. Clark, A. E. E. Rogers, J. D. Romney, A. R. Thompson, and R. C. Walker, “The Very Long Baseline Array,” *IEEE Proceedings*, vol. 82, pp. 658–672, May 1994.
- [32] R. N. Manchester, G. B. Hobbs, A. Teoh, and M. Hobbs, “The australia telescope national facility pulsar catalogue,” *The Astronomical Journal*, vol. 129, p. 1993–2006, Apr 2005.
- [33] D. R. Lorimer and M. Kramer, *Handbook of Pulsar Astronomy*. 2012.

- [34] A. T. Deller, W. M. Goss, W. F. Brisken, S. Chatterjee, J. M. Cordes, G. H. Janssen, Y. Y. Kovalev, T. J. W. Lazio, L. Petrov, B. W. Stappers, and et al., “Microarcsecond vlbi pulsar astrometry with psr ii. parallax distances for 57 pulsars,” *The Astrophysical Journal*, vol. 875, p. 100, Apr 2019.
- [35] M. Geyer and A. Karastergiou, “The frequency dependence of scattering imprints on pulsar observations,” *Monthly Notices of the Royal Astronomical Society*, vol. 462, pp. 2587–2602, 07 2016.
- [36] J. M. Cordes and T. J. W. Lazio, “NE2001. II. Using Radio Propagation Data to Construct a Model for the Galactic Distribution of Free Electrons,” *arXiv e-prints*, pp. astro-ph/0301598, Jan. 2003.
- [37] J. M. Cordes and T. J. W. Lazio, “NE2001.I. A New Model for the Galactic Distribution of Free Electrons and its Fluctuations,” *arXiv e-prints*, pp. astro-ph/0207156, July 2002.
- [38] J. M. Yao, R. N. Manchester, and N. Wang, “A new electron-density model for estimation of pulsar and frb distances,” *The Astrophysical Journal*, vol. 835, p. 29, Jan 2017.
- [39] N. Pol, S. Burke-Spolaor, N. Hurley-Walker, H. Blumer, S. Johnston, M. Keith, E. F. Keane, M. Burgay, A. Possenti, E. Petroff, and et al., “The location of young pulsar psr j0837–2454: Galactic halo or local supernova remnant?,” *The Astrophysical Journal*, vol. 911, p. 121, Apr 2021.

- [40] D. Altadill, A. Segarra, E. Blanch, J. M. Juan, V. V. Paznukhov, D. Buresova, I. Galkin, B. W. Reinisch, and A. Belehaki, "A method for real-time identification and tracking of traveling ionospheric disturbances using ionosonde data: first results," *Journal of Space Weather and Space Climate*, vol. 10, p. 2, Dec. 2020.
- [41] B. S. Arora, J. Morgan, S. M. Ord, S. J. Tingay, M. Bell, J. R. Callingham, K. S. Dwarakanath, B. Q. For, P. Hancock, L. Hindson, N. Hurley-Walker, M. Johnston-Hollitt, A. D. Kapińska, E. Lenc, B. McKinley, A. R. Offringa, P. Procopio, L. Staveley-Smith, R. B. Wayth, C. Wu, and Q. Zheng, "Ionospheric Modelling using GPS to Calibrate the MWA. II: Regional Ionospheric Modelling using GPS and GLONASS to Estimate Ionospheric Gradients," , vol. 33, p. e031, July 2016.
- [42] B. Arora, J. Morgan, S. Ord, S. Tingay, M. Bell, J. Callingham, K. Dwarakanath, B. For, P. Hancock, L. Hindson, N. Hurley-Walker, M. Johnston-Hollitt, A. Kapinska, E. Lenc, B. Mckinley, A. Offringa, P. Procopio, L. Staveley-Smith, R. Wayth, and Q. Zheng, "Ionospheric modelling using gps to calibrate the mwa. ii: Regional ionospheric modelling using gps and glonass to estimate ionospheric gradients," *Publications of the Astronomical Society of Australia*, vol. 33, 05 2016.
- [43] E. Ros, J. Marcaide, J. Guirado, E. Sardon, and I. Shapiro, "A gps-based method to model the plasma effects in vlbi observations," *Astronomy and Astrophysics*, vol. 356, 02 2000.

-
- [44] C. H. Jordan, S. Murray, C. M. Trott, R. B. Wayth, D. A. Mitchell, M. Rahimi, B. Pindor, P. Procopio, and J. Morgan, “Characterization of the ionosphere above the Murchison Radio Observatory using the Murchison Widefield Array,” *Monthly Notices of the Royal Astronomical Society*, vol. 471, pp. 3974–3987, 07 2017.
- [45] K. Bandura, A. N. Bender, J. F. Cliche, T. de Haan, M. A. Dobbs, A. J. Gilbert, S. Griffin, G. Hsyu, D. Ittah, J. M. Parra, J. Montgomery, T. Pinsonneault-Marotte, S. Siegel, G. Smecher, Q. Y. Tang, K. Vanderlinde, and N. Whitehorn, “Ice: a scalable, low-cost fpga-based telescope signal processing and networking system,” 2016.
- [46] A. E. Süzer and H. Oktal, “Prn code correlation in gps receiver,” in *2017 8th International Conference on Recent Advances in Space Technologies (RAST)*, pp. 189–193, 2017.
- [47] S. Raghavan, M. Shane, and R. Yowell, “Spread spectrum codes for gps l5,” in *2006 IEEE Aerospace Conference*, pp. 7 pp.–, 2006.
- [48] C. Fernández-Prades, J. Arribas, P. Closas, C. Avilés, and L. Esteve, “Gnss-sdr: An open source tool for researchers and developers,” vol. 2, 09 2011.